AGU PUBLICATIONS

Water Resources Research

RESEARCH ARTICLE
10.1002/2014WR015825

# Sediment transport and shear stress partitioning in a vegetated flow

**Caroline Le Bouteiller[1,2,3] and J. G. Venditti[1]**

[1]Department of Geography, Simon Fraser University, Burnaby, British Columbia, Canada, [2]IRSTEA, UR ETNA, Grenoble, France, [3]Université Grenoble Alpes, Grenoble, France

**Key Points:**
- Skin friction and sediment transport are reduced in a vegetated flow
- This reduction depends on the vegetation density
- Several methods for shear stress partitioning are tested and evaluated

**Correspondence to:**
C. Le Bouteiller,
caroline.le-bouteiller@irstea.fr

**Citation:**
Le Bouteiller, C., and J. G. Venditti (2015), Sediment transport and shear stress partitioning in a vegetated flow, *Water Resour. Res.*, *51*, doi:10.1002/2014WR015825.

Received 13 MAY 2014
Accepted 29 MAR 2015
Accepted article online 3 APR 2015

**Abstract** Vegetation is a common feature in natural coastal and riverine water ways, interacting with both the water flow and sediment transport. However, the physical processes governing these interactions are still poorly understood, which makes it difficult to predict sediment transport and morphodynamics in a vegetated environment. We performed a simple experiment to study how sediment transport responds to the presence of flexible, single-blade vegetation, and how this response is influenced by the vegetation density. We found that the skin friction and sediment transport are reduced in a plant patch, and that this effect is larger for denser vegetation. We then evaluated several methods to calculate the skin friction in a vegetated flow, which is the key to sediment transport prediction. Among these, the inversion of bed load transport formulas and the *Einstein and Banks* (1950) methods appeared to produce the most reasonable values of the skin friction. Finally, we suggest using the parameter $\alpha$, which is the ratio of the skin friction computed by these methods to the total bed shear stress, to make more realistic sediment transport predictions in morphodynamic models.

## 1. Introduction

Vegetation is a common feature in lowland rivers, estuaries, and tidal environments, and is a critical factor for the morphological evolution of such systems. In riverine environments, floodplain and riparian vegetation has been shown to contribute to bank cohesion and exerts a major control on channel geometry [*Tal and Paola*, 2007; *Gran and Paola*, 2001; *Li and Xie*, 2011], while controlling overbank deposition patterns during floods [*Perignon et al.*, 2013]. Observations in salt marshes suggest that vegetation tends to increase deposition, a process by which the marsh can grow [*Friedrichs and Perry*, 2001; *Bos et al.*, 2007; *Bouma et al.*, 2007] and persist with a rising sea level. In large-scale models of tidal evolution, vegetation is generally accounted for by increasing deposition [*Temmerman et al.*, 2007; *Kirwan and Murray*, 2007; *D'Alpaos et al.*, 2007; *Marani et al.*, 2010] and is shown to have a major influence on the long-term evolution of such systems. Recent investigations also suggest that the deposition patterns of suspended sediment and sediment transport rates are governed by the changes in the velocity and turbulence fields induced by vegetation [*Zong and Nepf*, 2011; *Follett and Nepf*, 2012; *Chen et al.*, 2012; *Yager and Schmeeckle*, 2013; *Le Bouteiller and Venditti*, 2014]. Not only do the interactions between vegetation and sediment transport control the morphological evolution of these systems but they also modify their ecological properties by creating specific habitats characterized by local sediment grain size, turbidity, and velocity gradients [*Madsen et al.*, 2001; *Sand-Jensen*, 1998; *Koch*, 2001] or controlling the transport of nutrients, seeds, or pollutants [*Chambers and Prepas*, 1994; *Moore*, 2004; *Brookshire and Dwire*, 2003]. Taking into account the effect of vegetation on sediment transport is therefore of critical importance for predicting the morphological and ecological trajectories of riverine and coastal vegetated systems. However, little is known about the quantitative properties of sediment transport through vegetation.

Sediment transport is driven by the flow, and more specifically by near-bed shear stress and turbulence. Therefore, the first element needed to quantify sediment transport in a vegetated flow is to understand the impact of vegetation on flow properties. This has been the focus of a large body of literature from the last decades [*Fonseca et al.*, 1982; *Raupach et al.*, 1996; *Wu et al.*, 1999; *Nepf and Vivoni*, 2000; *Ghisalberti and Nepf*, 2002; *Stephan and Gutknecht*, 2002; *Jarvela*, 2002; *Carollo et al.*, 2002; *Poggi et al.*, 2004; *Nepf*, 2012]. Vegetation growing on the bed of a river channel exerts a drag on the flow that reduces velocities. In the

case of a free-surface flow, this means that for a given discharge, the water depth will be higher in presence of vegetation than on a smoother bed. In a 2-D depth-averaged description of the flow, vegetation can therefore be accounted for by an increased friction coefficient. For instance, increased values of the Mannings coefficient for the design of waterways in presence of vegetation were proposed by *Ree* [1949, 1954].

However, the effect of the vegetation—particularly submerged vegetation—is also three dimensional. Not only does it increase the mean water depth for a given discharge, but it also modifies the vertical structure of the flow. Recent studies have shown through experimental [*Fonseca et al*., 1982; *Nepf and Vivoni*, 2000; *Carollo et al*., 2002; *Stephan and Gutknecht*, 2002; *Lefebvre et al*., 2010; *Chen et al*., 2011; *Folkard*, 2011; *Ghisalberti and Nepf*, 2006; *Bouma et al*., 2007; *Jarvela*, 2005] and field measurements [*Lacy and Wyllie-Echeverria*, 2011] that vertical velocity and turbulence profiles are modified by vegetation. For submerged vegetation, the flow is partitioned between a slow-moving zone inside the vegetation and a fast-moving zone above it. The velocity profile above the canopy can be described by modified versions of the logarithmic law [*Stephan and Gutknecht*, 2002; *Abdelrhman*, 2003; *Fischenich*, 1997; *Jarvela*, 2005], where the roughness height is adjusted to account for the vegetation. Velocity profiles tend to exhibit an inflection point at the top of the canopy, corresponding to the transition between this logarithmic shape and reduced velocity in the canopy. The difference between the upper and lower velocities is affected by the plant density [*Poggi et al*., 2004]. The high level of shear at the interface between the slow and fast-moving fluids can generate turbulence patterns that propagate along the top of the canopy, according to the Kelvin Helmholtz instability [*Nepf and Vivoni*, 2000]. This corresponds to a peak in the Reynolds shear stress at the top of canopy [*Nezu and Onitsuka*, 2001; *Nepf and Vivoni*, 2000]. In the case of flexible vegetation, a periodic waving of the canopy called monami has also been observed, in response to and interacting with the turbulent structures generated [*Okamoto et al*., 2012; *Nepf and Ghisalberti*, 2008].

Such modifications of the flow are expected to affect sediment transport, both as bed load and suspended load. While sediment transport is generally considered to be driven by the shear stress at the bottom of the flow, this bottom shear stress is extremely difficult to quantify in the presence of vegetation. In typical depth-averaged descriptions of the flow, the shear stress at the bottom can be extracted using a friction coefficient, assuming that this coefficient incorporates a unique source of friction located at the bottom of the flow. In a vegetated flow, the friction coefficient incorporates not only the friction at the bottom (the so-called "skin friction") but also the drag generated by the vegetation through the water column. Understanding the partitioning of the friction exerted on the flow by the various sources of drag is therefore critical for reasonable sediment transport prediction.

To bridge this gap, this paper aims to provide tools to estimate the skin friction and the sediment transport in vegetated flow. This requires a physical understanding of the relation between hydrodynamics and sediment transport at the plant patch scale. To further this understanding, we created a physical model of a plant patch and measured the flux of sediment transported through it, while varying the plant density within the patch. While studies with real vegetation have demonstrated how the flow response was influenced by vegetation shape, flexibility, and other properties [*Jarvela*, 2002; *Stephan and Gutknecht*, 2002], we chose to use a simple single-blade flexible model to isolate the effect of the vegetation on shear stress and sediment transport. This experiment was previously used by *Le Bouteiller and Venditti* [2014] to explore the morphodynamic response of a sand bed to the presence of dense vegetation. Here we focus on sediment transport and stress partitioning in the vegetated flow, with sparse and dense vegetation. Our specific research questions are: (1) how does sediment transport respond to vegetation? (2) How can we predict the skin stress? (3) What are the implications for the morphodynamic modeling of sediment transport? Our experiments demonstrate that sediment transport capacity is reduced in the plants due to a reduction of the skin friction. We then present and evaluate a series of methods that can be used to partition the shear stress, which allows reliable estimation of the skin stress hence sediment transport prediction.

## 2. Experimental Methods

### 2.1. Experimental Setup

Experiments were performed in a 15 m long, 1 m wide, tilting flume, located in the River Dynamics Laboratory at Simon Fraser University. The flume recirculates both water and sediment through two variable speed pumps. The central section of the flume located between 5 and 11 m was covered with a vegetated bed

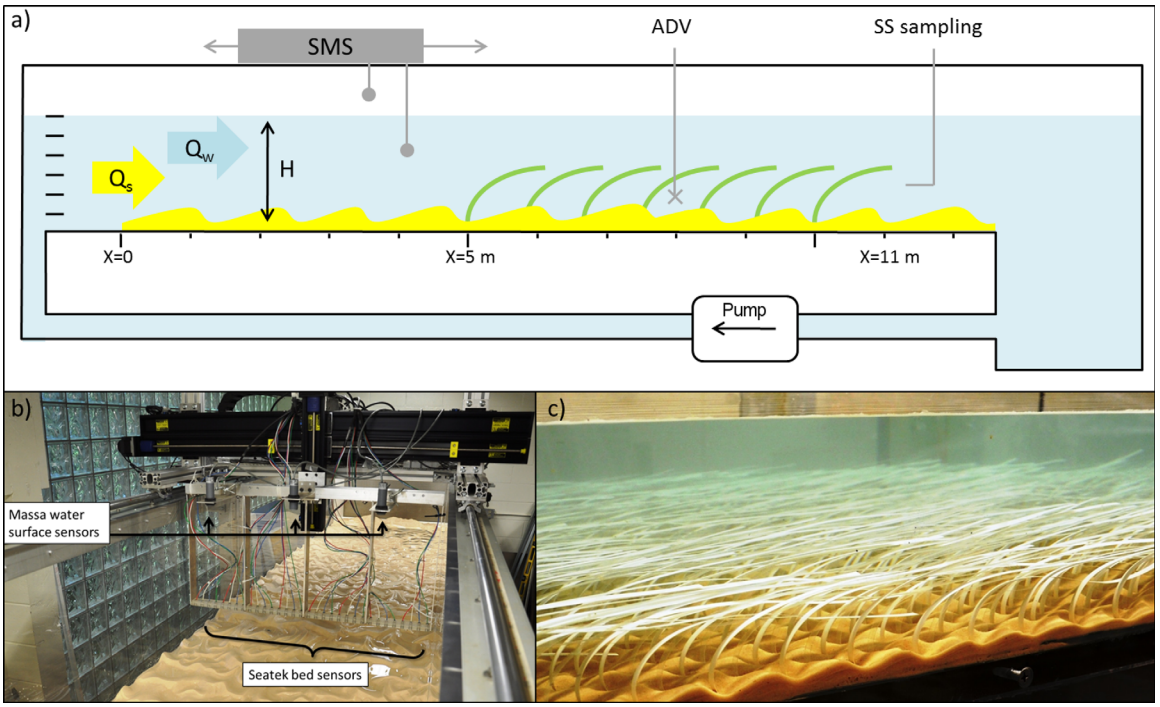


**Figure 1.** (a) Sketch of the 12 m flume in the River Dynamics Laboratory at Simon Fraser University showing the plant patch, the robotic Swath Mapping System (SMS), and the measurement devices. (b) Robotic swath mapping system used for bed and water surfaces scans. (c) Photograph of the experiment with dense vegetation and Flow 2, flow is from left to right.

(see Figure 1) made up of artificial plant blades in staggered arrays. Each plant was made of one blade which was taped on the plastic bottom. Following *Ghisalberti and Nepf* [2002], blade material and dimensions were chosen to ensure similarity to natural eelgrasses by maintaining the ratio of the flexural rigidity and buoyancy forces. The blades were made of low-density (920 kg $m^{-2}$) polyethylene film with a Young modulus of $2 \times 10^8$ Pa and were 25.5 cm long, 0.75 cm wide, and 0.2 mm thick. Two plant densities were used in the experiments: 130 and 800 blades per square meter of bed. The common measure used for canopy density is the frontal area per canopy volume $a$. Assuming that each blade oriented itself normal to the flow, the theoretical frontal area in our experiments is the product of the blade width by the plant density, which is $a$=0.01 $cm^{-1}$ for the low density and $a = 0.06$ $cm^{-1}$ for the high-density patch. The low-density value is at the low end of observed densities of coastal eelgrass *Zostera marina* on the tidal flats of Southwestern Canada, while the high density is midrange of observed densities (C. Durance, Precision Identification, personal communication, 2011). Following *Dunn and Garcia* [1996] and *Poggi et al*. [2004], the effect of the vegetation on the flow structure depends on the value of $C_p a h_p$ (where $C_p$ is the plant drag coefficient and $h_p$ the plant deflected height) and is noticeable only for $C_p a h_p \geq 0.1$. Assuming $C_p = 1$ as suggested by *Nepf and Vivoni* [2000], and with $h_p = 5$–10 cm, the low density selected for the experiment corresponds to $C_p a h_p = 0.05$–0.1 while the high density corresponds to $C_p a h_p = 0.3$–0.6.

Approximately 420 kg of sand were introduced in the flume to produce a bed of thickness ranging from 2 to 3 cm, which covered the flume bottom, but was not so thick that the plants were buried. The median grain size of the sand ($D_{50}$) was 150 $\mu$m and it had a narrow grain size distribution (the ninetieth and tenth percentiles were 230 and 90 $\mu$m). After the sand was inserted into the flume and before the experiments, the sand was recirculated for a few hours to ensure that the system reached an equilibrium configuration where the amount of sand deposited in the flume plumbing system (end tank and supply pipes) did not vary. This ensures that the amount of sand injected upstream is equal to the amount of sand which is exported downstream of the flume.

### 2.2. Experimental Procedure

For each plant density, we performed three experimental runs, varying the water discharge (0.035, 0.04, and 0.05 $m^3$ $s^{-1}$) were used (Table 1). The water depth was kept constant at approximately 15 cm by adding or

**Table 1.** Flow and Sediment Transport Conditions at Equilibrium

| | | Q ($m^3/s$) | h (m) | U (m/s) | Fr[a] | Re[a] | $Re_g$[a] | $S_b$ | $S_w$ | $Q_{sb}$ (g/s) | $Q_{ss}$ (g/s) | $\tau$ (Pa) | $\tau^*$ |
|---|---|---|---|---|---|---|---|---|---|---|---|---|---|
| Sparse Plants | Flow 1 | 0.05 ± 1% | 0.146 ± 2% | 0.34 ± 3% | 0.28 | 49504 | 7.17 | 0.0018±2% | 0.0016 ±0.7% | 1.79 ± 6% | 5.22 ± 13% | 2.37±3% | 0.98 |
| | Flow 2 | 0.04 ± 1% | 0.146 ± 2% | 0.27 ± 3% | 0.23 | 39312 | 6.71 | 0.0024 ± 2% | 0.0014±0.9% | 0.68 ± 6% | 0.39 ± 24% | 1.93 ± 3% | 0.79 |
| | Flow 3 | 0.034 ± 1% | 0.152 ± 2% | 0.22 ± 4% | 0.18 | 33396 | 6.07 | 0.0003 ± 17% | 0.0011 ±0.8% | 0.03 ± 4% | 0.25 ± 31% | 1.51 ± 3% | 0.62 |
| Dense Plants | Flow 1 | 0.05 ± 1% | 0.136 ± 5% | 0.37 ± 6% | 0.32 | 50283 | 8.83 | 0.0077 ±0.4% | 0.0024±0.5% | 1.96 ± 6% | 2.71 ± 14% | 3.78 ± 7% | 1.56 |
| | Flow 2 | 0.04 ± 1% | 0.142 ± 5% | 0.28 ± 6% | 0.24 | 39676 | 8.10 | 0.0063 ± 1% | 0.0021 ± 1% | 0.35 ± 8% | 0.31 ± 28% | 3.23 ± 7% | 1.33 |
| | Flow 3 | 0.035 ± 1% | 0.153 ± 2% | 0.23 ± 3% | 0.19 | 35282 | 6.10 | 0.0026±2% | 0.0011 ± 1% | 0.14 ± 7% | 0.13 ± 41% | 1.58 ± 3% | 0.65 |

[a] $Fr = U/\sqrt{hg}$; $Re = Uh/\nu$; $Re_g = \sqrt{ghS_w}D_{50}/\nu$.

removing water in the system between each run. The flow velocities therefore ranged from 0.20 to 0.33 m $s^{-1}$ (Table 1), which are characteristic values for flows on tidal flats where *Zostera marina* are found (D. Ray, Northwest Hydraulic Consultants Ltd., personal communication, 2012).

Flows were fully turbulent and subcritical in terms of the Froude numbers and hydraulically transitional between rough and smooth boundary flow (Table 1). The transport stage in the experiments, calculated as the ratio between the Shields number and critical Shields number, ranged between 7 and 20, which corresponds to a mixed (bed load and suspended load) transport stage [*Church*, 2006] with an increasing suspended component with increasing discharge.

In a recirculating flume, the water discharge $Q$ and the water depth $h$ are fixed, while the sediment transport rate $Q_s$ and the bed slope $S_b$ are free to adjust. Both $Q_s$ and $S_b$ were measured during the experiments. Each experiment started with a flat bed and was run until a morphodynamic equilibrium was reached, where the sediment discharge was uniform through the flume, which corresponded to steady state bed topography.

### 2.3. Measurements

We measured water surface and bed elevations using a robotic Swath Mapping System (SMS) that traverses the flume on rails attached to the top of the tank (see Figure 1). The SMS consists of (1) a 32 transducer Seatek Instruments echo-sounding system (accuracy ±1 mm); (2) 5 MassaSonic ultrasonic sensors (accuracy ±2 mm); (3) a mechanical stepper-motor-driven arm that moves sensors vertically; (4) a mechanical, stepper-motor-driven system that moves the SMS in the streamwise direction; and (5) an onboard computer that records all sensor signals and positions. The ultrasonic sensors measure water surface elevations. The Seatek transducers, which measure bed elevation, are mounted in a Plexigas beam, oriented across the channel, with a spacing of 2.5 cm.

For each bed elevation measurement, the transducer beam was lowered a few millimeters below the water surface. In our experiments, we used the middle 30 Seatek transducers ($y = 6$–$94$ cm, from the right-hand flume wall, looking downstream) and the channel center ultrasonic sensor. The velocity of the SMS was chosen such that the downstream spacing of the measurements was 1 mm for the bed scans and 3 mm for the water surface scans.

Bed surface scans were filtered using three sequential filters. The first removed points that were in the water column or below the flume bottom. The second used a threshold in $\partial z/\partial x$ to remove points that corresponded to a strong and localized change in the bed elevation. The third removed points that departed too much from the local mean elevation of the bed. Parameters for each of these filters were adjusted based on the bed and plant properties in order to retain signal variability related to the small-scale bed forms, but to remove the peaks related to the plants.

Bed slopes $S_b$ were calculated from the cross-stream average of 30 alongstream profiles measured with the echo sounders. To avoid the transitory effects observed at the entrance of the plants and possible backwater effects at the end of the flume, the bed slope in the plant patch was evaluated over a 4 m section of the flume (from 6 to 10 m). In the low-density runs, the occurrence of alternate bars necessitated calculation of the bed slope along the thalweg (using the lowest point of each cross section) rather than the bed slope averaged over the cross section. The water surface slopes $S_w$ were calculated from the cross-stream average of the three ultrasonic water surface probes over the same distance used for $S_b$. The uncertainty on $S_b$ and $S_w$ was estimated as the error from the linear regression. Because of the variability of sediment transport

even at steady state, we expect that the bed slope $S_b$ could vary by as much as a few percent about its steady state value. Unfortunately this source of uncertainty could only be quantified using a large number of measurements at steady state, which were not taken.

The mean flow depth was first estimated visually using rulers on the flume glass walls then calculated from the difference between the cross-stream averaged water surface and bed surface profiles. Uncertainty of the depth measurement was taken as the standard deviation of this difference. The water discharge was measured with a flowmeter (accuracy $\pm 0.0005$ $m^3/s$), and the mean velocity was obtained by dividing the discharge by the water depth and flume width.

Vertical velocity profiles were measured at approximately 3 m into the plant patch, along the centerline, with a Nortek Vectrino Accoustic Doppler velocimeter (ADV) at 50 Hz. At this location, the profiles are expected to be fully developed; *Chen et al*. [2013, equation (10)] predicts an adjustment length scale of 0.83 m for our experiments [*Le Bouteiller and Venditti*, 2014]. Velocity profiles were collected at the end of each experiment, once the morphology had stabilized. The first point was collected approximately 1.5 mm above the bed, and vertical spacing for the points in the profiles was 3 mm in the canopy region and 6 mm far above the canopy. For each point, data were collected for at least 60 s—the minimum duration needed for the turbulence statistics to converge. Profiles were collected either (1) above one plant blade (2) between plant blades or (3) in a gap made in the canopy by removing a few plant blades. Profiles in case (1) show a similar flow field to case (2) above the canopy but could not be used for the flow in the canopy. In case (3), sediment deposition in the hole indicated that the flow and turbulence properties were different from those inside the canopy. Ultimately we report only profiles from case (2), where it was possible to filter out the abnormal values corresponding to a waving plant passing into the measurement region. One such profile was used for each run.

Bed load transport rates were measured by collecting and weighing the sand exiting the channel in a 32 by 18 cm mesh-bottomed box at the outlet of the flume over periods that ranged from 0.5 to several hours (depending on the transport rate). Suspended sediment was measured 50 cm before the flume outlet using an L-shaped, 6.35 mm copper tube attached at an isokinetic pump, at 4, 8, and 12 cm above the bed for the low-density plants and 2, 4, 8, and 12 cm above the bed for the high-density plants. One liter samples were collected at each location, corresponding to a sampling time of 1.5–6 min. The water samples were then filtered and the filters weighed to get the suspended sediment concentrations. Suspended sediment load was estimated by depth-averaging the measured concentrations. Uncertainty on bed load and suspended load transport rates was estimated by combining all sources of uncertainty in the sampling and weighing procedure. Observed values of bed load and total load transport rates were compared to predictions using bed load transport formulas [*Wilson*, 1966; *Ashida and Michiue*, 1972; *Engelund and Fredsoe*, 1976; *Fernandez-Luque and Van Beek*, 1976; *Van Rijn*, 1984; *Nino and Garcia*, 1998] and total load transport formulas [*Engelund and Hansen*, 1967; *Ackers and White*, 1973; *Brownlie*, 1981].

As the blade waving made it difficult to measure the plant deflected height, we used the location of the peak in the Reynolds stress profile (see section 3.3) as an estimation of the plant height. The values we obtained by this method are consistent with our casual observations during the experiments. However, note that the peaks in the Reynolds stress profiles for the sparse vegetation are very poorly defined, so we estimate that the uncertainty in plant height in this case as $\pm 10$ mm.

## 3. Experimental Results

### 3.1. Morphodynamic Evolution of the Bed

Figure 2 shows the morphodynamic evolution of the bed through time for two flows in the sparse and dense vegetation. There were some important differences in the way the bed evolved between the two plant densities. In the high-density case, a scour zone formed at the entrance of the plant patch, followed by a sand deposit immediately downstream that grew through time, eventually reaching an equilibrium morphology that increased the bed slope through the plant patch. A second sand deposit formed at the exit to the plant patch. In the low-density case, there was only a slight scouring effect at the entrance of the patch, but the bed remained relatively flat in general. A similar scour zone at the entrance of a plant patch was observed in experiments by *Chen et al*. [2012]. However, the dimensions of the scour zone in their experiments were found to decrease with the vegetation density, contrary to what our experiments suggest.

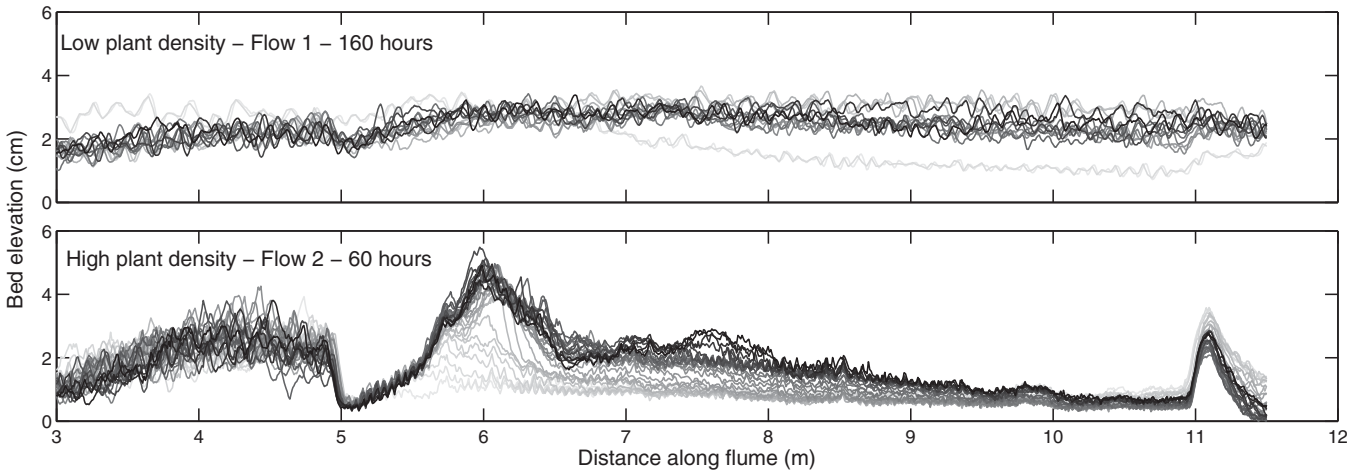


**Figure 2.** Examples of bed evolution from gray (original bed) to black lines (steady state) for (a) low plant density and Flow 1 over 160 h, with one scan every few hours, and (b) high plant density and Flow 2 over 60 h, with one scan every 2 h. High-density data from *Le Bouteiller and Venditti* [2014]. Note that the elevation is measured in the reference of the flume, so the slope is relative to the flume bottom.

*Le Bouteiller and Venditti* [2014] showed that the initial scour zone is related to the fluid deceleration and stem-generated turbulence induced by the high velocity entering the patch. They also showed that in the high-density runs, the overall increase in bed and water surface slope through the plant patch allowed for the imposed sediment load to be passed through the plant patch. This morphodynamic adjustment to the plants occurred because the plants extract momentum from the flow, reducing grain-related shear stress responsible for moving sediment.

The pattern of ripples, which develop almost immediately at the beginning of each run (see Figure 2), also differed between the two densities. While ripples formed both upstream and through the plant patch at both densities, in the low-density runs, ripples were roughly the same size (height $\Delta = 15$, 8, and 10 mm for the highest, medium, and lowest flows, respectively) in and outside of the plant patch and the ripples migrated through the plant patch. In the high-density runs the ripples were forced by the plant stems and were larger upstream of the plant patch (up to 20 mm) than within it ($\Delta = 12$, 6, and 5 mm for the highest, medium, and lowest flows, respectively) due to the lower shear stress applied to the bed. Alternate bars formed in the low-density case, even though the width to depth ratio ($\approx 6.6$) is well outside the optimal range suggested for bar topography to develop [*Colombini et al*., 1987].

In most experiments, the topography tended to stabilize after a few hours or days, while the bed load flux variability decreased. An example of the time evolution of the bed slope ($S_b$), water surface slope ($S_w$), and sediment flux at the flume outlet ($Q_s$) is given in Figure 3.

### 3.2. Flow Conditions

Flow and sediment transport conditions at equilibrium are summarized in Table 1. The bed and water surface slopes in the experiments increased with discharge for both plant densities. Because of the abrupt transition between the unvegetated and vegetated sections of the bed, the bed and water surface slope did not match perfectly. The subparallel water and bed surfaces caused some convective acceleration through the eelgrass. So we used the 1-D shallow-water momentum equation to calculate the total bed stress with a convective acceleration term (see *Le Bouteiller and Venditti* [2014] for complete derivation)

$$\tau = \rho g h S_w + \rho U^2 \partial h / \partial x = \rho g h S_w + \rho U^2 (S_b - S_w) \quad (1)$$

where $\rho$ is the density of water, $g$ is gravitational acceleration, $U$ is the streamwise depth-averaged velocity, $h$ is the water depth, and $x$ is distance along the flume. Uncertainty in $\tau$ was estimated by combining the uncertainties from all variables in equation (1). We also applied the sidewall correction to the water depth from *Vanoni and Brooks* [1957]. Since the bed with plants and sand was much rougher than the glass sidewalls, the effect of the wall correction is not substantial (3–6%). In the sparse plant

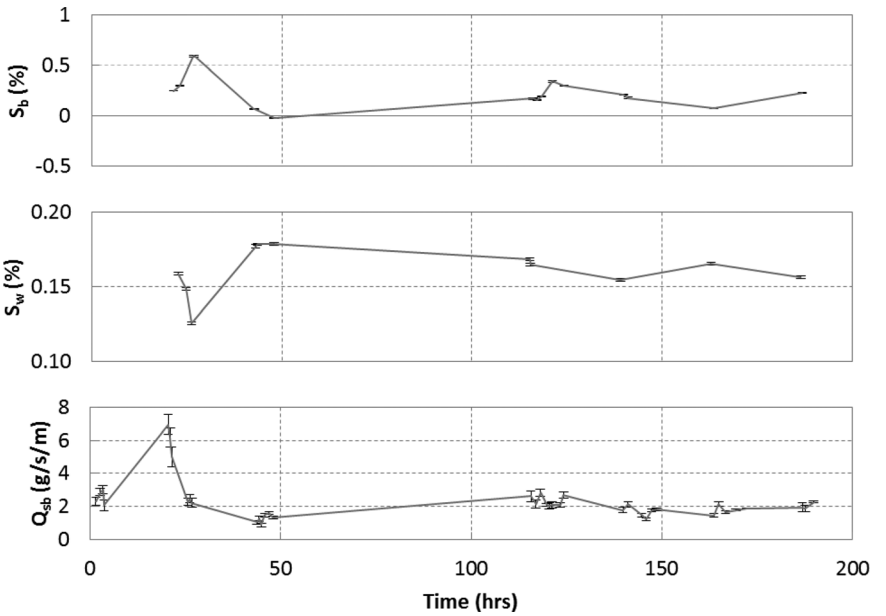


**Figure 3.** Time evolution of bed slope $S_b$, water surface slope $S_w$, and bed load transport rate $Q_{sb}$ for Flow 1 with low plant density. Error is less than 1% for $S_w$, between 1 and 10% for $S_b$, and between 5 and 15% for $Q_{sb}$.

patch, convective acceleration accounts for 3, 4, and 1% of the total bed stress for the lowest, medium, and highest flow, respectively. In the dense patch, it accounts for 2, 10, and 18% of the total bed stress. The total bed stress increased with discharge and was higher for the dense plants than for the sparse plants, because the change in slope that occurred to pass the incoming sediment supply through the plants was larger.

### 3.3. Velocity Profiles

Velocity and turbulence profiles capture the impact of the bed forms and plants on the flow field (Figure 4).

For the high-density cases, the mean streamwise velocity profiles have two well-defined inflection points at approximately 20 and 40 mm above the bed. The profiles of Reynolds shear stress and of the horizontal turbulent intensity both present a major peak at approximately 40 mm above the bed (50 mm for Flow 3) and a smaller one at 7.5 mm above the bed for Flows 1 and 2.

The shape of the velocity profiles for high density is characteristic of a flow within a canopy and has been observed in both field and laboratory experiments [*Nepf and Vivoni*, 2000; *Carollo et al*., 2002; *Lacy and Wyllie-Echeverria*, 2011], for water as well as airflows [*Brunet et al*., 1994]. The highest inflection point corresponds to the location of the top of the canopy [*Nezu and Onitsuka*, 2001; *Nepf and Vivoni*, 2000] and is the consequence of the difference between the velocity in and above the canopy. This velocity differential generates a shear interface that triggers Kelvin-Helmoltz instabilities. The presence of the inflection point in the velocity profile has been shown to be a necessary condition for the development of such an instability [*Raupach and Thom*, 1981; *Raupach et al*., 1996]. The growth of Kelvin-Helmoltz vortices at the top of the canopy is in turn reflected in the peak in the turbulence intensity and in the Reynolds shear stress profiles [*Nepf and Vivoni*, 2000; *Ghisalberti and Nepf*, 2006]. The peak in these profiles is located approximately at the top of the canopy [*Nezu and Onitsuka*, 2001; *Chen et al*., 2011; *Carollo et al*., 2002; *Bouma et al*., 2007].

For the low-density cases, the mean streamwise velocity profiles deviate only slightly from the semilogarithmic shape of a rough flow ($R^2 = 0.91$, 0.98, and 0.91, respectively, for Flows 1–3). The Reynolds shear stress and the horizontal turbulent intensity (root mean square of the fluctuating velocity) are nearly constant over the depth, with a small peak at approximately 7.5 mm above the bed for Flows 1 and 2. The absence of an inflection point in the velocity profile and of a clear peak in Reynolds stresses indicates that the vegetation density is not high enough to generate a shear layer, consistently with what was predicted using the $h_p * a * C_p$ threshold from section 2.1.

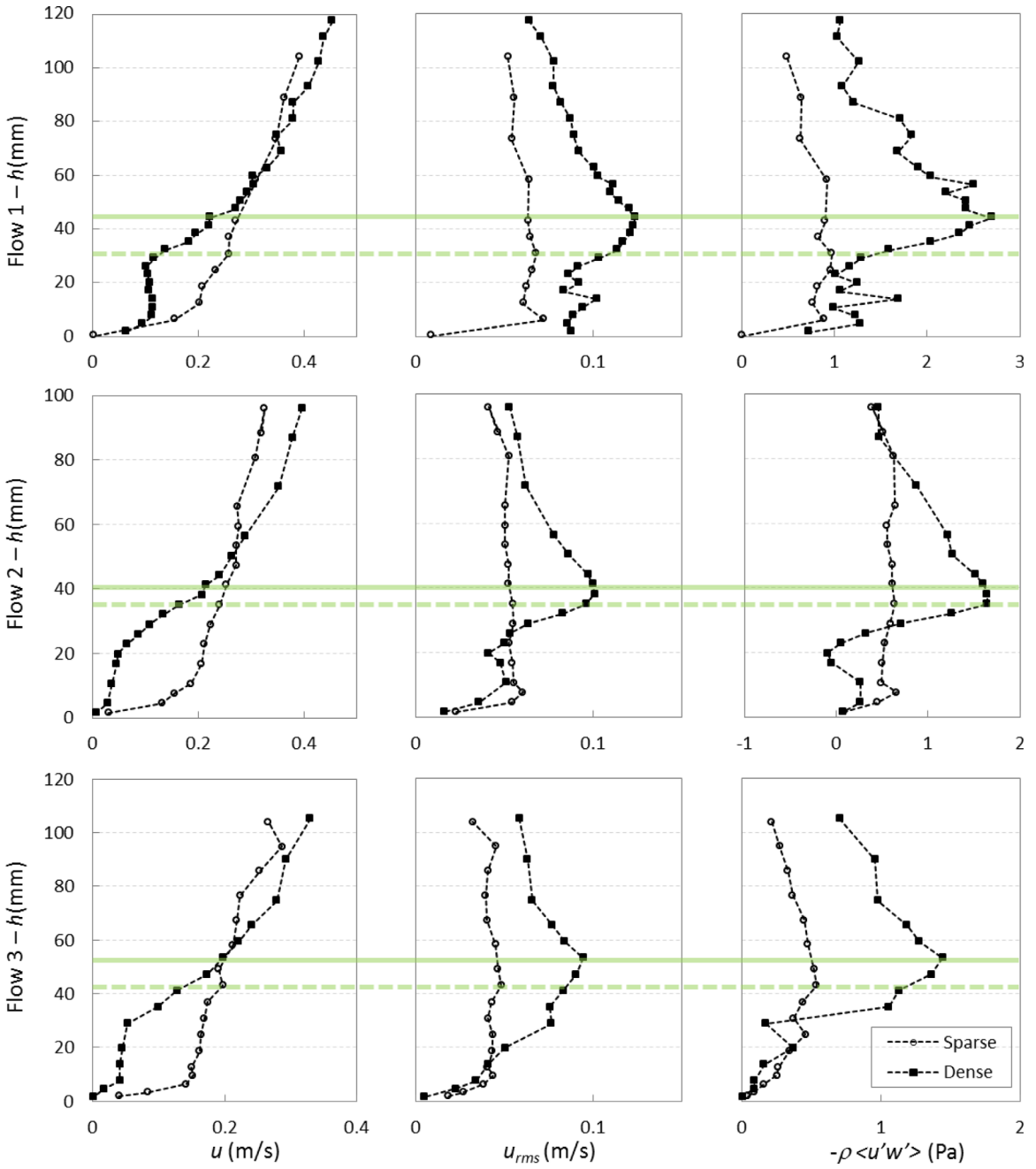


**Figure 4.** Profiles of mean streamwise velocity $u$, root mean square of streamwise velocity $u_{rms}$, and Reynolds shear stress ($-\rho < u'w' >$) for all flows, in sparse and dense plant patches. Green lines indicate the canopy height $h_p$ for the dense vegetation (full lines) and for the sparse vegetation (dotted lines).

On the other hand, the small peak in Reynolds shear stress and turbulence intensity that is observed close to the bed in the low-density profiles indicates that turbulence is generated in this region, which is a signature of the bed forms. Indeed, the height of the bed forms measured from bed scans (see section 3.1) corresponds to the location of the peak. Detailed studies of the flow structure over bed forms [*Wiberg and Nelson*, 1992; *Nelson et al*., 1993] have shown that Reynolds stress profiles averaged over a dune or ripple field have a distinct peak corresponding to flow separation in the lee of ripples and dunes.

This peak is also observed for the high-density profiles, suggesting that turbulence is also generated by the bed forms in this case. This peak has a lower amplitude than the low-density one, which is probably related

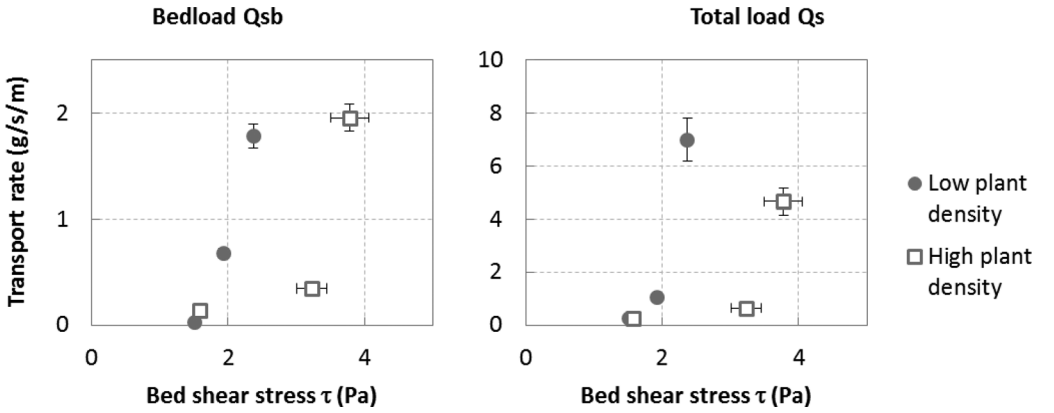


**Figure 5.** Sediment transport rate as measured at the flume outlet as a function of the total bed stress $\tau$ in the plants. When no error bar is visible, error is smaller than the symbol.

to the reduced velocity in this region. The Reynolds stress and velocity profiles therefore capture the role of both the vegetation and the bed forms in the structure of the flow.

### 3.4. Sediment Transport

For each plant density, bed load and suspended load transport rates increase with water discharge (Table 1). All cases correspond to a mixed transport stage, with an increasing contribution of the suspended load for the highest discharge (58 and 74% of the total load for the dense and sparse case, respectively). A minor decrease in sediment transport suggests that it is inhibited by vegetation. For bed load with Flow 1, and for suspended load with Flow 2, the difference in transport rates between the sparse and dense cases is less than the measurement uncertainty. However, for bed load with Flow 2, and for suspended load with Flows 1 and 3, the transport rates in the sparse patch are twice as high as in the dense patch. Finally, bed load transport rate with Flow 3 in the dense patch is more than 4 times higher than in the sparse patch, but this difference is not very meaningful because this case is near the sediment entrainment threshold, and the flow was not fixed at exactly the same value in the sparse and dense experiment (0.034 versus 0.035 $m^3/s$). In Figure 5, the bed load transport and total load transport rates that were measured at the flume outlet are plotted as a function of the total bed stress computed in the plants. Bed load and total load increase with the total bed stress, and two different trends appear clearly for the sparse and dense vegetation.

The total bed stress computed from equation (1) is a total value that integrates all the possible sources of friction on the flow. More specifically, it incorporates the grain-related stress, which is the shear stress applied to the grains that induces sediment transport, as well as the form drag exerted on the flow by the bed forms and by the plants. Note that strictly speaking, the grain-related stress is the sum of the skin stress on the surface of the grains and of the form drag generated at the scale of each individual grain. However, the grain-related stress is commonly referred to as the "skin friction" in the literature and we will use this convention in the following. We therefore expect that the total bed stress computed from equation (1) is not appropriate for sediment transport prediction [cf. *Larsen et al.*, 2009; *Yager and Schmeeckle*, 2013], and we tested this assumption with formulas for total load and bed load transport.

Total load and bed load predictions are shown in Figure 6. For the total load prediction, all three formulas overpredict the total load, and the overprediction is larger in the dense vegetation. As these formulas were calibrated to nonvegetated flows, this indicates that for similar mean flow conditions, vegetation tends to decrease the sediment transport. Moreover, this effect is stronger for denser vegetation. For the bed load prediction, all formulas overpredict the bed load by 1–3 orders of magnitude. Similar results have been presented by *Yager and Schmeeckle* [2013]. Sediment transport, both as bed load and total load, is therefore lower within the plant patch than what would be expected in a nonvegetated flow. A more realistic prediction of the sediment flux in the plants, therefore, requires separation of the skin

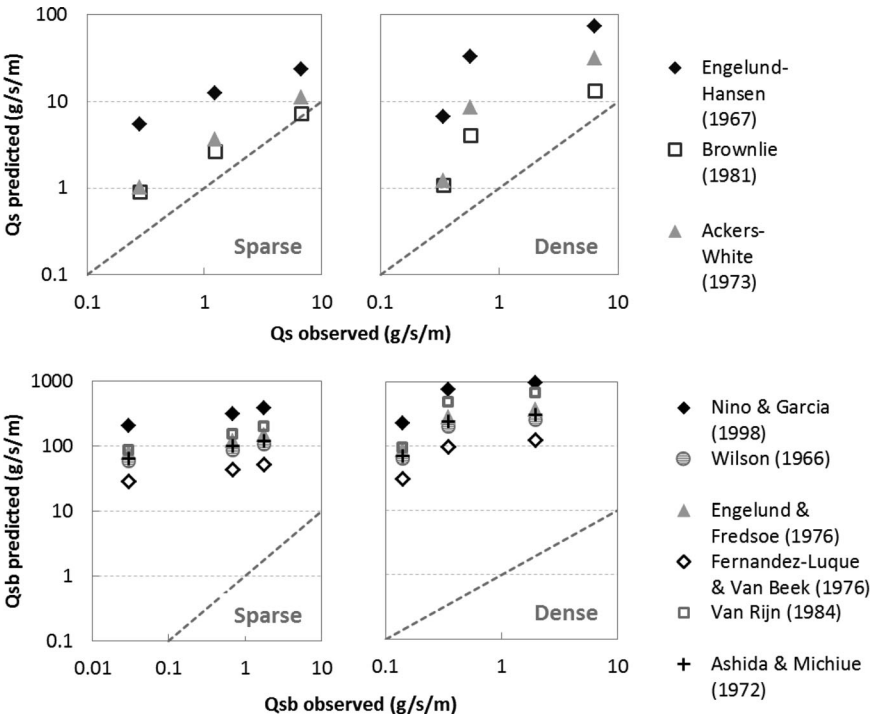


**Figure 6.** Predicted versus observed total load $Q_s$, and predicted versus observed bed load $Q_{sb}$, according to several transport formulas, for (left) sparse and (right) dense cases (data for dense case is from *Le Bouteiller and Venditti* [2014]).

friction component and the plant and bed form drag from the total bed stress value [*Jordanova and James*, 2003; *Wu and He*, 2009].

## 4. Shear Stress Partitioning Methods

In the following, we will present and discuss seven different methodologies for partitioning the total bed stress among these three components, according to the following equation:

$$\tau = \tau_s + \tau_p + \tau_{bf} \tag{2}$$

where $\tau_s$ is the skin friction, $\tau_p$ is the form drag due to the plant, and $\tau_{bf}$ is the form drag due to the bed forms. We introduce the parameter $\alpha$, which is the ratio of the skin friction to the total bed stress, so that

$$\alpha = \frac{\tau_s}{\tau} = \frac{\tau - \tau_p - \tau_{bf}}{\tau} \tag{3}$$

This parameter $\alpha$ will be used in the following to compare the different partitioning methods. The results of each partitioning method are presented in section 5.

### 4.1. Inversion of a Bed Load Transport Formula

A simple method that can be used to extract the skin friction component from the experiments is to search for the value of the shear stress that would lead to a bed load transport rate similar to our measurements in the absence of any plants or bed forms. Contrary to the total load transport formulas presented above, bed load transport formulas are not based on the total bed stress and mean flow properties but rather on the skin friction component. We selected six bed load transport formulas that have been designed or used for sand transport (see section 2.3). We then computed the skin friction accordingly. The critical Shields parameter that is needed for such calculations was either taken as 0.05 as recommended for *Ashida and Michiue* [1972], *Engelund and Fredsoe* [1976], and *Fernandez-Luque and Van Beek* [1976] formulas, or computed according to *Brownlie*'s [1981] equation, which yields a value of 0.067, in the other cases. For each bed load formula, the uncertainty on $\tau_s$ was estimated using the lower and upper error bounds on $Q_{sb}$. The

uncertainty in $\alpha$ was then calculated combining the standard deviation of $\tau_s$ values over all methods with the uncertainty in $\tau$.

### 4.2. Einstein Partitioning Method

*Einstein and Banks* [1950] partitioned the total bed stress $\tau$ between the skin friction component and the form drag. Although this method was not designed specifically for vegetated beds, it does not require any assumption about the origin of the form drag. Therefore, it is applicable in our case where the form drag is the result of both bed forms and plants. The total bed stress is calculated as:

$$\tau = \rho g h S = \rho C_f U^2 \tag{4}$$

where $C_f$ is the total resistance coefficient. The skin friction is associated with the resistance coefficient $C_{fs}$ due to skin friction only and the equilibrium water depth $H_s$ that would be obtained at the same velocity $U$ but in the absence of any vegetation form drag.

$$\tau_s = \rho g H_s S = \rho C_{fs} U^2 \tag{5}$$

The skin friction coefficient $C_{fs}$ can be expressed as a function of $H_s$ using Keulegan resistance law for rough turbulent flows:

$$C_{fs} = \left[\frac{1}{\kappa} \ln\left(\frac{11 H_s}{k_s}\right)\right]^{-2} \tag{6}$$

where the grain roughness $k_s = 2.5 D_{50}$. Combining equations (5) and (6), it is possible to calculate the value of $H_s$ and $\tau_s$. Error bounds on $\tau_s$ values were calculated using the least favorable combination of errors in $h$, $Q$, and $S_w$. Error bounds on $\alpha$ values are calculated using the least favorable combination of errors in $\tau_s$ and $\tau$.

### 4.3. Extension of the Smith and McLean [1977] Method

*Smith and McLean* [1977] and later *Wiberg and Nelson* [1992] developed a method for partitioning the total bed stress between a form drag induced by bed forms and a skin friction. Here we follow the same framework to extend this method to a case with an added source of form drag from the plants. Following *Smith and McLean* [1977], the stress induced by the bed forms is written:

$$\tau_{bf} = \frac{1}{2} \rho C_{bf} U_{bf}^2 \frac{\Delta}{\lambda} \tag{7}$$

where $C_{bf}$ is the drag coefficient for the bed forms, $\Delta$ and $\lambda$ are the bed forms height and length, $U_{bf}$ is the mean velocity that would prevail for $k_s < z < \Delta$ in the absence of bed forms. Assuming a logarithmic velocity profile, $U_{bf}$ is then given by:

$$U_{bf} = \frac{\sqrt{\tau_s/\rho}}{\kappa}\left(\ln\frac{30\Delta}{k_s} - 1\right) \tag{8}$$

Similarly, one can define the shear stress induced by the plants as the drag force due to the plants divided by a unit bed area:

$$\tau_p = \frac{1}{2} \rho C_p U_p^2 a h_p \tag{9}$$

$C_p$ is the drag coefficient for the plants, $a$ is the frontal area per canopy volume, and $h_p$ is the plant height, which varies with the velocity. We define $U_p$ as the mean velocity that would prevail for $k_s < z < h_p$ in the absence of vegetation, which can be calculated as:

$$U_p = \frac{\sqrt{\tau_s/\rho}}{\kappa}\left(\ln\frac{30 h_p}{k_s} - 1\right) \tag{10}$$

Combining equations (2), (7), and (9) yields the following expression that relates the total bed stress to the skin friction:

$$\tau=\tau_s\left[1+\frac{C_{bf}}{2\kappa^2}\frac{\Delta}{\lambda}\left(\ln\frac{30\Delta}{k_s}-1\right)^2+\frac{C_p}{2\kappa^2}ah_p\left(\ln\frac{30h_p}{k_s}-1\right)^2\right] \quad (11)$$

In order to compute the skin friction from equation (11), values of the ripple height ($\Delta$) and length ($\lambda$), plant deflected height $h_p$, and of the drag coefficients $C_{bf}$ and $C_p$, are needed. The values of $\Delta$ and $\lambda$ are measured from the bed scans and $h_p$ is estimated from the velocity and Reynolds stress profile inflection point highest in the flow (Table A3).

It is theoretically possible to compute $C_p$ from Reynolds stresses profiles using the horizontally averaged momentum equation [*Nepf and Vivoni*, 2000; *Dunn and Garcia*, 1996] at every depth $z$ within the vegetated region ($\Delta < z < h_p$):

$$0=gS-\frac{\partial<u'w'>}{\partial z}-\frac{1}{2}\rho C_p a u^2(z) \quad (12)$$

This procedure was applied to our data but yields values of $C_p$ are unrealistically high (as high as 9) and not correlated over the depth. This can reasonably be attributed to insufficient vertical resolution in the ADV profiles and to the nonuniformity of the flow. We decided instead to use $C_p = 1$, which is the value reported by *Nepf and Vivoni* [2000] for submerged flexible vegetation. For the bed form drag coefficient $C_{bf}$, we use as a first approximation the value of 0.17 obtained by *Wiberg and Nelson* [1992] for asymmetric ripples. Uncertainty on $\tau_s$ and $\alpha$ values is estimated using the least favorable combination of errors on $h_p$, $\Delta$, $\lambda$, and $\tau$.

### 4.4. Explicit Formulation of Each Friction Term

An alternative approach to the *Smith and McLean* [1977] method described above is to define the velocity term in equations (7) and (9) using the measured velocity profiles. Here $U_{bf}$ is the mean velocity over the water depth occupied by the bed forms ($k_s < z < \Delta$), and $U_p$ is the mean velocity averaged over the water depth occupied by the plants ($k_s < z < h_p$). Combining equations (2), (7), and (9) yields the following expression that relates the skin friction to the total bed stress:

$$\tau=\tau_s+\frac{1}{2}\rho C_{bf}\frac{\Delta}{\lambda}U_{bf}^2+\frac{1}{2}\rho C_p a h_p U_p^2 \quad (13)$$

In equation (13), all friction components are defined explicitly, based on local variables that can be measured. The third term on the right-hand side that refers to the vegetation drag is similar to what was proposed by *Larsen et al.* [2009] for emerged vegetation. Note, however, that *Larsen et al.* [2009] formulation accounts for a drag coefficient $C_p$ and a plant frontal area $a$ that vary with $z$ (which is needed for real plants) while we use constant values corresponding to the simpler morphology of our artificial plants. The total bed stress components are computed using the same hypothesis as previously for the form drag coefficients $C_p$ and $C_{bf}$. Uncertainty on $\tau_s$ and $\alpha$ values was estimated using the least favorable combination of errors on $h_p$, $\Delta$, $\lambda$, $U_p$, $U_{bf}$, and $\tau$.

### 4.5. Estimation of the Shear Velocity From the Velocity Profiles

In a rough turbulent flow, the mixing length theory predicts a logarithmic shape for the velocity profile, based on the hypothesis that the mixing length is proportional to the distance from the bed $z$. The mixing length can roughly be seen as the size of the largest eddies at a given depth, which is likely to be controlled by the smallest length scale in the flow. On a rippled and vegetated bed, the three main length scales are the distance of the point of interest to the bed, the ripple dimension (length/height) and the spacing between the plants. It is therefore expected that in a region close enough to the bed, the smallest length scale is $z$, so the mixing length is controlled by the distance to the bed just as in a nonvegetated flow, resulting in a logarithmic shape of the near-bed velocity profile. For each velocity profile, we selected the region close to the bed where the profile can be considered to be logarithmic, i.e., where the mixing length theory can be used to extract the shear velocity $u*$ from the profile with $u* = \kappa \cdot \partial u(z)/\partial \ln z$. The number of points used for the logarithmic fit, the corresponding height above the bed and the $R^2$ value for the fit are indicated in Appendix 1, Table A5. The skin friction is computed as $\tau_s=\rho u*^2$. Uncertainty on $u*$ and $\tau_s$ was

estimated as the error from the semilogarithmic regression. Note, however, that the variability of the flow field at the stem scale could also induce some uncertainty on the measurement of the velocity profiles, which we could not quantify here.

### 4.6. Estimation of the Bottom Shear Stress From the Reynolds Stress Profiles

Another way to estimate skin shear stresses is directly from the Reynolds stress profiles. The shear stress distribution in a flow is given by:

$$\tau(z)=\rho\left(\nu\frac{\partial u}{\partial z}-<u'w'>\right) \tag{14}$$

where $\nu$ is the kinematic viscosity of water ($\approx 1\times10^{-6}$). The first term on the right-hand side is negligible and the shear stress is approximately equal to $-\rho<u'w'>$. The skin friction should be equivalent to the Reynolds stress close to the boundary, but not on the bed itself where continuity imposes $<u'w'>=0$. To avoid as much as possible both the damping of the turbulence by the vicinity of the bed and the changes in the profiles due to the bed forms, we averaged $<u'w'>$ over the first 5 mm (first two points) of the profiles to estimate the skin friction. The uncertainty of this measurement is therefore of the order of half of the difference between those two values.

### 4.7. Raupach [1992] and Shao and Yang [2008] Method

*Raupach* [1992] proposed a method for partitioning the drag for atmospheric flow over a rough surface. From the characterization of effective shelter area and shelter volume behind a rough element, the following expression was derived to relate the surface stress (skin friction) to the total bed stress:

$$\frac{\tau_s}{\tau}=\frac{1}{1+\frac{C_r}{2C_{fs}}ah_p} \tag{15}$$

Here $C_{fs}$ is the resistance coefficient corresponding to the skin friction only, as defined in equation (6), and $C_r$ is the drag coefficient associated with the roughness elements. If the drag induced by the bed forms is small compared to the drag induced by the plants, $C_r$ can be replaced by $C_p$ in equation (15). The *Raupach* [1992] partitioning method was based on the assumption that the sheltering from each roughness element do not interact with each other, which restrains the applicability of the method to low plant densities only. *Shao and Yang* [2008] therefore proposed a correction to the method that allows for higher densities, which leads to the following expression:

$$\frac{\tau_s}{\tau}=\frac{1}{1+e^{2ah_p}\frac{C_r}{2C_{fs}}ah_p} \tag{16}$$

Equation (16) predicts a smaller contribution of the skin friction at high plant densities than equation (15). Combining equations (5), (6), and (16), we solve for the value of $H_s$ to obtain the values of $\tau_s$. The uncertainty on $\tau_s$ and $\alpha$ is estimated from the least favorable combination of errors on $h_p$ an $\tau$.

## 5. Shear Stress Partitioning Results

Results from all partitioning methods are summarized in Table 2.

### 5.1. Inversion of a Bed Load Transport Formula

Results from the inversion of the six bed load formulas are detailed in Appendix A, Table A1. Values of $\tau_s$ range from 0.13 to 0.39 Pa, with little variability among the six formulas. Averaging over the six bed load formulas, the skin friction estimate for the sparse vegetation with Flows 1–3 is, respectively, $0.30\pm0.06$, $0.23\pm0.04$, and $0.16\pm0.03$ Pa, while for the dense vegetation, it is, respectively, $0.30\pm0.06$, $0.20\pm0.03$, and $0.17\pm0.03$ Pa. The general trend is that the ratio $\alpha$ is higher for lower plant density, because of the lower form drag generated by the vegetation (Table 2). The mean value of $\alpha$ in the sparse vegetation is $11.5\%\pm2.4$, and in the dense vegetation, it is $8.4\%\pm2$. $\alpha$ also increases with the velocity (except for the case of Flow 3 with high density), although this increase is within the error range. This could be caused by a decrease of the form drag due to the bending of the flexible vegetation, as observed by *Jarvela* [2002].

**Table 2.** Values of $\alpha=\tau_s/\tau$ (in %) Obtained With All the Methods Tested

| | | Bed Load Formulas | Einstein and Banks | Extension of Smith and Mclean | Explicit Computation | Log Fit Velocity Profile | Reynolds Stress Profile | Shao and Yang | Avg. | Std. |
|---|---|---|---|---|---|---|---|---|---|---|
| Sparse Plants | Flow 1 | 13 | 20 | 11 | 77 | 39 | 12 | 17 | 27 | 24 |
| | Flow 2 | 12 | 17 | 14 | 70 | 51 | 14 | 18 | 28 | 23 |
| | Flow 3 | 10 | 15 | 11 | 65 | 62 | 5 | 15 | 26 | 26 |
| Dense Plants | Flow 1 | 8 | 15 | 2 | 33 | 4 | 19 | 3 | 12 | 11 |
| | Flow 2 | 6 | 11 | 3 | 66 | 1 | 5 | 3 | 14 | 23 |
| | Flow 3 | 11 | 15 | 2 | 36 | 4 | 3 | 3 | 11 | 12 |

### 5.2. Einstein Partitioning Method

This method yields values of skin stress $\tau_s$ ranging between 0.22 and 0.48 Pa (Appendix A, Table A2). The skin stress increases with the flow velocity. Corresponding $\alpha$ values range between 11.4 and 20.1% (Table 2). Except for Flow 3 in the dense patch, the ratio $\alpha$ of the skin friction to the total bed stress increases with the velocity. It is also higher for the lowest plant density. Averaging over the three flows, the skin friction represents 17.1 $\pm$ 2.0% of the total bed stress for the low plant density and 13.8 $\pm$ 1.6% for the high plant density.

### 5.3. Extension of the Smith and McLean [1977] Method

The primary contribution to the total bed stress comes from the vegetation-induced form drag (Appendix A, Table A3). This contribution represents 55–95% of the total bed stress (Table 2) and is higher in the higher-density patch (average of 90%) than in the lower density patch (average of 62%). It also appears that the contribution of the plant-induced form drag is higher at low velocities, when the plants bend less and occupy more space in the flow. The second greatest contribution to the total bed stress is form drag induced by the ripples. This contribution ranges from 3% to 34% and is substantially higher for the lower-density patch. This is consistent with our observations that ripples are constrained by the vegetation and tend to be smaller in the high-vegetation patch. Finally, the contribution of the skin friction predicted by this partition method is very low, from 2 to 14% of the total bed stress.

The skin friction values are much lower than those predicted by other methods. In particular, the values predicted for the high-density patch correspond to Shields numbers of 0.012–0.033, which are lower than the critical Shields number estimated as 0.067 from *Brownlie* [1981] and should not induce any sediment transport. We interpret this to mean that the skin friction is underestimated by this method. One possible reason is that the procedure adopted here treats the effect of the bed forms and plants independently, whereas there are likely some interactions between these effects. Sheltering of the bottom of a plant by a ripple might be expected, in cases where a plant is growing close or in the bed form. In order to evaluate this effect, the above procedure has been modified by removing the contribution of the plants for $k_s < z < \Delta$. This corresponds to a case where all the blades are always growing on the highest points of the bed forms, which is the extreme case of sheltering. Such a modification yields slightly higher values of the skin friction contribution (2–16%). Another reason for underestimating the skin friction is that the estimation of the reference velocities based on a logarithmic profile yields values that are higher than the actual velocities in the plants. The form drag terms, which are a function of the velocity squared (equations (7) and (9)), are therefore overestimated with this method.

**Table A1.** Skin Friction Values Obtained by Inverting Bed Load Transport Formulas in Order to Match the Observed Sediment Transport Rate

| | | $\tau_s$ (Pa) | | | | | | | | |
|---|---|---|---|---|---|---|---|---|---|---|
| | | Nino and Garcia [1998] | Ashida and Michiue [1972] | Wilson [1966] | Engelund and Fredsoe [1976] | Fernandez-Luque and Van Beek [1976] | Van Rijn [1984] | Avg. (Pa) | Std. (Pa) | $\alpha=\tau_s/\tau$ (%) |
| Sparse Plants | Flow 1 | 0.22 $\pm$ 0.003 | 0.30 $\pm$ 0.006 | 0.29 $\pm$ 0.006 | 0.24 $\pm$ 0.005 | 0.34 $\pm$ 0.009 | 0.38 $\pm$ 0.006 | 0.30 | 0.06 | 12.5 $\pm$ 2.7 |
| | Flow 2 | 0.19 $\pm$ 0.001 | 0.22 $\pm$ 0.003 | 0.23 $\pm$ 0.003 | 0.18 $\pm$ 0.003 | 0.24 $\pm$ 0.005 | 0.30 $\pm$ 0.004 | 0.23 | 0.04 | 11.8 $\pm$ 2.5 |
| | Flow 3 | 0.16 $\pm$ 0.000 | 0.14 $\pm$ 0.000 | 0.17 $\pm$ 0.000 | 0.13 $\pm$ 0.000 | 0.14 $\pm$ 0.000 | 0.19 $\pm$ 0.000 | 0.16 | 0.03 | 10.3 $\pm$ 2.0 |
| Dense Plants | Flow 1 | 0.23 $\pm$ 0.003 | 0.30 $\pm$ 0.006 | 0.30 $\pm$ 0.006 | 0.25 $\pm$ 0.005 | 0.35 $\pm$ 0.010 | 0.39 $\pm$ 0.007 | 0.30 | 0.06 | 8.0 $\pm$ 2.2 |
| | Flow 2 | 0.18 $\pm$ 0.001 | 0.19 $\pm$ 0.003 | 0.21 $\pm$ 0.002 | 0.16 $\pm$ 0.002 | 0.19 $\pm$ 0.004 | 0.26 $\pm$ 0.004 | 0.20 | 0.03 | 6.2 $\pm$ 1.5 |
| | Flow 3 | 0.17 $\pm$ 0.000 | 0.17 $\pm$ 0.001 | 0.19 $\pm$ 0.001 | 0.14 $\pm$ 0.001 | 0.16 $\pm$ 0.002 | 0.23 $\pm$ 0.002 | 0.17 | 0.03 | 11.1 $\pm$ 2.3 |

**Table A2.** Skin Friction Values Obtained From the *Einstein and Banks* [1950] Partitioning Method

| | | $\tau_s$ (Pa) | $\alpha=\tau_s/\tau$ (%) |
|---|---|---|---|
| Sparse Plants | Flow 1 | 0.48 (0.46–0.5) | 20.1 (18.8–21.5) |
| | Flow 2 | 0.32 (0.30–0.33) | 16.5 (15.3–17.9) |
| | Flow 3 | 0.22 (0.21–0.24) | 14.8 (13.5–16.2) |
| Dense Plants | Flow 1 | 0.58 (0.52–0.64) | 15.2 (12.9–18.3) |
| | Flow 2 | 0.37 (0.33–0.41) | 11.4 (9.7–13.6) |
| | Flow 3 | 0.23 (0.22–0.24) | 14.7 (13.4–16.1) |

### 5.4. Explicit Formulation of Each Friction Term

This method produces $\tau_s$ values of 1.83, 1.31, and 0.98 Pa for Flows 1–3 in the sparse vegetation, and 1.26, 2.12, and 0.56 Pa for Flows 1–3 in the dense patch (Appendix A, Table A4). In the dense patch, the plant-induced form drag is the main component of the total bed stress (53 $\pm$ 12%) whereas in the sparse patch, the skin friction is the most important component (71 $\pm$ 4%). In both cases, the bed form-induced form drag is negligible (0–6%), due to the fact that the velocity close to the bed is so low. $\alpha$ values range from 33 to 77% according to this method (Table 2) and there is no clear effect of the velocity on these values.

### 5.5. Estimation of the Shear Velocity From the Velocity Profiles

This method yields values of the skin friction $\tau_s$ of 0.04–0.14 Pa in the dense patch, and 0.91–0.98 Pa in the sparse patch (Appendix A, Table A5). There is clear effect of the vegetation density on the $\alpha$ ratio (Table 2). On average, the skin friction represents 3 $\pm$ 1% of the total bed stress in the dense patch, and 50 $\pm$ 8% in the sparse patch. Contrary to what was obtained with the Einstein and transport formula methods, in the sparse patch, $\alpha$ is higher for lower flow velocities, and this trend is more substantial than the uncertainty of the calculations.

### 5.6. Estimation of the Bottom Shear Stress From the Reynolds Stress Profiles

This method yields values of the skin friction $\tau_s$ of 0.29, 0.26, and 0.07 Pa for Flows 1–3 in the sparse patch, and 0.72, 0.16, and 0.05 Pa for Flows 1–3 in the dense patch (Appendix A, Table A6). The $\alpha$ values range from 3 to 19% (Table 2). Due to the calculation method for $\tau_s$, there is a high uncertainty on the values produced by this method. No trend of $\alpha$ varying with the flow velocity or with the vegetation density can be detected within this uncertainty.

### 5.7. Raupach [1992] and Shao and Yang [2008] Method

The Raupach method yields values of the skin friction $\tau_s$ that range between 0.06–0.17 Pa for the dense patch and 0.25–0.42 Pa for the sparse patch (Appendix A, Table A7). The Shao and Yang method yields only slightly lower values of $\tau_s$. $\alpha$ ranges from 3 to 18% (Table 2). There is a clear effect of the plant density on $\alpha$. For the Raupach method, the skin friction represents on average 4.4 $\pm$ 0.3% and 17.4 $\pm$ 0.8% of the total bed stress in the dense and sparse patch, respectively. Compared to the Raupach method, the Shao and Yang correction yields values of $\alpha$ that are slightly lower in the sparse patch (16.5 $\pm$ 0.8%) and about on third lower in the dense patch (3.0 $\pm$ 0.3%). Note that the values of skin friction predicted for the lowest flows in the dense patch (Appendix A, Table A7) correspond to Shields numbers that are too small to trigger sediment transport (0.016 and 0.045 for Flows 3 and 2, respectively). There is no clear effect of the flow velocity on $\alpha$.

### 5.8. Trends From All Methods

All results for the calculation of the $\alpha$ ratio are summarized in Table 2 and Figure 7. The mean value of $\alpha=\tau_s/\tau$ based on all estimates is $\alpha=12\pm15\%$ in the dense patch and $27\pm23\%$ in the sparse patch.

We explore how $\alpha$ depends on the two quantities that were varied in our experiments: the flow velocity and the plant density. In Figure 8, the skin friction $\tau_s=\alpha*\tau$ is plotted as a function of the total bed stress $\tau$. For most cases, data points clearly differ for the sparse and dense vegetation, and a linear

**Table A3.** Shear Stress Partition Obtained by the Extension of the Smith and Mclean Method

| | | $\Delta$ (m) | $\lambda$ (m) | $h_p$ (m) | $\tau_s$ (Pa) | $\alpha=\tau_s/\tau$ (%) | $\tau_{bf}$ (Pa) | $\tau_{bf}/\tau$ (%) | $\tau_p$ (Pa) | $\tau_p/\tau$ (%) |
|---|---|---|---|---|---|---|---|---|---|---|
| Sparse Plants | Flow 1 | 0.015 $\pm$ 0.002 | 0.124 $\pm$ 0.001 | 0.037 $\pm$ 0.01 | 0.25 (0.20–0.35) | 10.7 (8.5–14.3) | 0.81 | 34.1 | 1.31 | 55.3 |
| | Flow 2 | 0.008 $\pm$ 0.002 | 0.124 $\pm$ 0.001 | 0.035 $\pm$ 0.01 | 0.27 (0.20–0.40) | 14.0 (10.6–20.0) | 0.37 | 19.2 | 1.29 | 66.8 |
| | Flow 3 | 0.01 $\pm$ 0.002 | 0.124 $\pm$ 0.001 | 0.043 $\pm$ 0.01 | 0.16 (0.12–0.21) | 10.6 (8.3–13.8) | 0.37 | 24.5 | 0.98 | 64.9 |
| Dense Plants | Flow 1 | 0.012 $\pm$ 0.002 | 0.05 $\pm$ 0.001 | 0.044 $\pm$ 0.003 | 0.08 (0.07–0.10) | 2.2 (2.0–2.5) | 0.49 | 13.0 | 3.21 | 84.9 |
| | Flow 2 | 0.006 $\pm$ 0.002 | 0.05 $\pm$ 0.001 | 0.041 $\pm$ 0.003 | 0.08 (0.07–0.10) | 2.5 (2.9–2.3) | 0.19 | 5.9 | 2.95 | 91.6 |
| | Flow 3 | 0.005 $\pm$ 0.002 | 0.05 $\pm$ 0.001 | 0.053 $\pm$ 0.003 | 0.03(0.03–0.03) | 1.9 (1.8–2.1) | 0.05 | 3.2 | 1.5 | 94.9 |

**Table A4.** Shear Stress Partitioning Obtained by Explicitly Defining Each Term, According to Equation (13)

| | | $U_p$ (m/s)[a] | $U_{bf}$ (m/s)[a] | $\tau_s$ (Pa) | $\alpha=\tau_s/\tau$ (%) | $\tau_{bf}$ (Pa) | $\tau_{bf}/\tau$ (%) | $\tau_p$ (Pa) | $\tau_p/\tau$ (%) |
|---|---|---|---|---|---|---|---|---|---|
| Sparse Plants | Flow 1 | 0.155 ± 0.003 | 0.095 ± 0.002 | 1.83 (1.61–2.04) | 77.3 (69.8–84.0) | 0.09 | 3.8 | 0.44 | 18.6 |
| | Flow 2 | 0.173 ± 0.003 | 0.105 ± 0.002 | 1.31 (1.09–1.59) | 69.7 (58.5–79.7) | 0.06 | 3.1 | 0.52 | 26.9 |
| | Flow 3 | 0.143 ± 0.002 | 0.104 ± 0.01 | 0.98 (0.80–1.16) | 65.0 (54.5–74.4) | 0.09 | 6.0 | 0.44 | 29.1 |
| Dense Plants | Flow 1 | 0.133 ± 0.01 | 0.096 ± 0.008 | 1.26 (0.35–2.07) | 33.3 (10.1–51.0) | 0.19 | 5.0 | 2.33 | 61.6 |
| | Flow 2 | 0.095 ± 0.005 | 0.018 ± 0.001 | 2.12 (1.68–2.52) | 65.5 (56–73.2) | 0.00 | 0.0 | 1.11 | 34.4 |
| | Flow 3 | 0.08 ± 0.004 | 0.009 ± 0.0003 | 0.56 (0.33–0.77) | 35.6 (22.0–47.2) | 0.00 | 0.0 | 1.02 | 64.6 |

[a]The reference velocity for the form drag terms is computed based on real velocity data.

relation appears when looking separately at each plant density. This indicates that $\alpha$ is independent of the flow velocity in the range of values tested, but highly dependent on the plant density. Such a conclusion is also supported by a statistical analysis of the numerical values from Table 2. A Student's *t* test using all $\alpha$ values that were produced indicates that the difference between the mean value of $\alpha$ obtained for the dense and sparse cases is statistically significant (at the 95% confidence level). On the contrary, the same test reveals that there is no significant difference between the mean values of $\alpha$ obtained for each flow.

## 6. Discussion

### 6.1. How Does Sediment Transport Respond to Vegetation?

Our observations indicate that there is a significant effect of vegetation on the sediment transport and morphodynamics and that this effect is higher for denser vegetation. Here we do not focus on the local scour effect at the entrance of the patch but rather on the general bed slope increase in the patch. More details on the morphologic adjustment in the dense patch can be found in *Le Bouteiller and Venditti* [2014, Figures 1 and 4]. Because of the drag generated by the plants, near-bed velocity and skin friction are reduced in the plant patch, so the sediment transport capacity is also reduced. Such reduction of the skin friction in the plant patch was observed in previous experimental and numerical findings [*Bouma et al*., 2007; *Souliotis and Prinos*, 2011]. The sand bed responds to this by an increase of the bed slope, which increases the skin friction and restores the sediment transport capacity needed to carry the imposed sediment flux. The sediment fluxes that are measured at equilibrium are therefore associated with different bed morphologies for the sparse and dense case. The equilibrium water and bed slopes are such that the skin friction is sufficient to transfer the sediment flux through the vegetated patch. At the beginning of the experiment in the dense vegetation, the plant drag is higher than in the sparse vegetation, so the reduction of the sediment transport capacity is more substantial. This results in more sediment deposition and leads to a higher equilibrium slope for the supplied sediment to be passed through the patch. Such deposition features and morphodynamic adjustments are consistent with previous experimental findings and field observations in salt marshes and seagrass meadows [*Fonseca et al*., 1983; *Bouma et al*., 2007; *Chen et al*., 2012].

Vegetation therefore affects sediment transport, and this is recorded in the resulting equilibrium morphology. The ratio of the skin friction to the total bed stress ($\alpha$), that defines how much near-bed shear stress is available to move the sediments in the plant patch, is the main factor that controls the final equilibrium slope. From our observations, $\alpha$ is clearly higher in the sparse than in the dense patch. Although we did not explicitly test this in our experiments, we expect that $\alpha$ does not depend only on the plant density, but

**Table A5.** Skin Friction Obtained by Log Fit on Velocity Profiles Close to the Bed

| | | $u^*$ (m/s) | $\tau_s$ (Pa) | $\alpha=\tau_s/\tau$ (%) | $R^2$ | No of Points Used for Fit | $h_{max}$ Used for Fit (mm)[a] |
|---|---|---|---|---|---|---|---|
| Sparse Plants | Flow 1 | 0.03 ± 0.003 | 0.91 ± 0.15 | 38.5 ± 7.4 | 0.94 | 10 | 18.3 |
| | Flow 2 | 0.032 ± 0.002 | 0.98 ± 0.15 | 50.8 ± 9.2 | 0.98 | 5 | 16.8 |
| | Flow 3 | 0.031 ± 0.003 | 0.93 ± 0.19 | 61.6 ± 14.8 | 0.98 | 4 | 9.5 |
| Dense Plants | Flow 1 | 0.012 ± 0.001 | 0.14 ± 0.03 | 3.7 ± 1.0 | 0.97 | 4 | 10.7 |
| | Flow 2 | 0.007 ± 0.0005 | 0.04 ± 0.01 | 1.2 ± 0.3 | 0.99 | 5 | 19.8 |
| | Flow 3 | 0.008 ± 0.002 | 0.07 ± 0.03 | 4.4 ± 2.3 | 0.9 | 4 | 13.7 |

[a]$h_{max}$ is the elevation above the bed of the highest point used for the fit.

**Table A6.** Skin Friction Values Obtained Using an Average of the Reynolds Shear Stress in the First 5 mm Above the Bed

| | | $\tau_s$ (Pa) | $\alpha=\tau_s/\tau$ (%) |
|---|---|---|---|
| Sparse Plants | Flow 1 | 0.29 ± 0.03 | 12.1 ± 1.5 |
| | Flow 2 | 0.26 ± 0.19 | 13.7 ± 10.0 |
| | Flow 3 | 0.07 ± 0.02 | 4.5 ±1.7 |
| Dense Plants | Flow 1 | 0.72 ± 0.36 | 19.0 ± 3.3 |
| | Flow 2 | 0.16 ± 0.10 | 5.1 ± 3.3 |
| | Flow 3 | 0.05 ± 0.04 | 3.0 ± 2.7 |

rather on the vegetation frontal area, which incorporates other vegetation characteristics such as the shape and the flexibility of the plants, as suggested by previous works [*Jarvela*, 2002]. Quantifying this $\alpha$ value requires a detailed analysis of the final morphology and stress patterns, which can be performed with the partitioning methods that were presented in section 4. In the following, we compare the methods and make some suggestions about which one(s) are the most appropriate to predict the skin stress.

### 6.2. What Is the Best Method to Predict the Skin Friction?

In the following, we test the reliability of the partitioning methods based on three criteria. First, a realistic partitioning should produce small enough values of $\alpha$ to account for the important contribution of the form drag generated by the plants. Using field velocity measurements, *Lacy and Wyllie-Echeverria* [2011] found that the drag coefficient $C_f$ (defined in equation (4)) was 3–8 times higher at eelgrass vegetated sites (with a plant density of 0.02 $cm^{-1}$ in the same range as our experimental values) than at an unvegetated site. The skin friction should be lower in the vegetated sites than in the unvegetated site, where it is approximately equal to the total stress ($\tau_s(veg) \leq \tau_s(unveg)=\tau(unveg)=1/8$ to $1/3 * \tau(veg)$). This provides a higher bound of 13–33% for $\alpha$ in eelgrass vegetation that we can use here. The bed load formulas [*Einstein and Banks*, 1950], the extension of *Smith and McLean* [1977], the Reynolds stress, and *Shao and Yang* [2008] methods all produce values of $\alpha$ that satisfy this criterion. On the contrary, the explicit computation and the logarithmic fit to the velocity profile in the sparse vegetation produce values of $\alpha$ that are always higher than 33% (Figure 7).

A second criterion is that an appropriate method should produce values of $\tau_s$ that increase with the bed load transport rate. The methods that respect this criterion are the bed load formulas, *Einstein and Banks* [1950], the Reynolds stress, and *Shao and Yang* [2008] (see Appendix A for values of $\tau_s$).

A third criterion is based on the dependency of $\alpha$ on the plant density. Figure 5 indicates that the relation between the total bed stress and the bed load transport rate is different for the sparse and dense vegetation cases. Assuming that bed load transport is driven by the skin friction, the relation between the skin friction and the bed load transport rate should be unique and independent on the plant density. This helps us define the third criterion for the validity of the partitioning methods that are tested and proposed. Let us call $\alpha_S$ and $\alpha_D$ the ratio of the skin friction to the total bed stress for the sparse and dense cases, respectively. In order to obtain a unique relationship between $\alpha_i * \tau$ and $Q_{sb}$ (where subscript $i$ is either $D$ or $S$). Figure 5 suggests that $\alpha_D$ should be smaller than $\alpha_S$. We look for the relationship between $\alpha_S$ and $\alpha_D$ that will provide the best collapse of all data points of Figure 5 on a unique trend $Q_{sb}=f(\alpha_i * \tau)$. Using several best fit procedures (based either on minimizing the sum of all the distances between points $(\tau_s, Q_{sb})$, fitting a line between these points, or fitting a transport formula with exponent 1.5 or 2 or with a free exponent), we found that the ratio $\alpha_D/\alpha_S$ should be 61–67%. This criterion does not yield the real value of the skin friction, but gives an indication of the influence of the plant density on the $\alpha$ ratio. Among all the methods tested, the following methods produce reasonable estimates of the ratio $\alpha_D/\alpha_S$: inversion of bed load formulas

**Table A7.** Skin Friction Values Obtained From the *Raupach* [1992] and *Shao and Yang* [2008] Methods

| | | Raupach [1992] | | Shao and Yang [2008] | |
|---|---|---|---|---|---|
| | | $\tau_s$ (Pa) | $\alpha=\tau_s/\tau$ (%) | $\tau_s$ (Pa) | $\alpha=\tau_s/\tau$ (%) |
| Sparse Plants | Flow 1 | 0.42 (0.35–0.53) | 17.7 (15.2–21.6) | 0.40 (0.33–0.51) | 16.8 (14.2–20.9) |
| | Flow 2 | 0.35 (0.29–0.45) | 18.3 (15.6–22.6) | 0.34 (0.28–0.44) | 17.5 (14.7–21.9) |
| | Flow 3 | 0.25 (0.21–0.30) | 16.2 (14.2–19.2) | 0.23 (0.19–0.29) | 15.3 (13.3–18.4) |
| Dense Plants | Flow 1 | 0.17 (0.15–0.19) | 4.5 (4.3–4.6) | 0.12 (0.10–0.13) | 3.1 (2.9–3.3) |
| | Flow 2 | 0.15 (0.14–0.17) | 4.7 (4.6–4.9) | 0.11 (0.10–0.12) | 3.3 (3.2–3.6) |
| | Flow 3 | 0.06 (0.06–0.07) | 4 (3.9–4.1) | 0.04 (0.04–0.05) | 2.6 (2.5–2.7) |

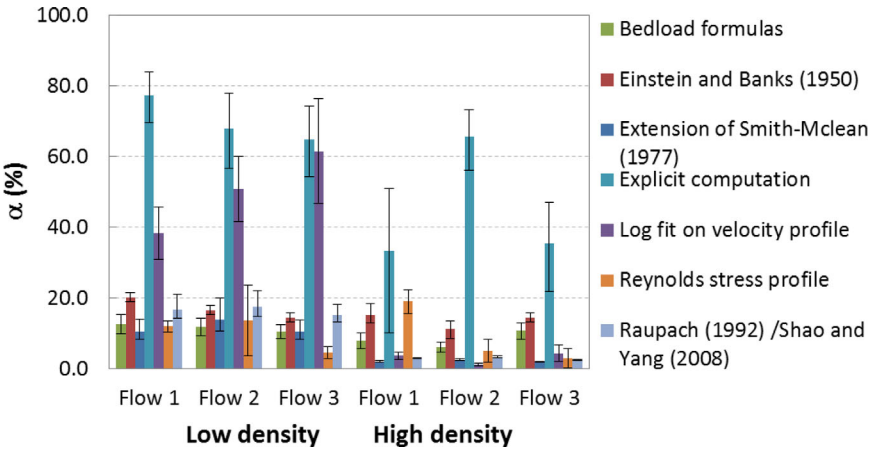


**Figure 7.** Comparison of $\alpha$ estimates obtained by all the methods tested.

[*Einstein and Banks*, 1950] and explicit computation ($\alpha_D/\alpha_S$ is, respectively, 71, 74, and 64%). On the other hand, the methods based on the *Smith and McLean* [1977] partition, the logarithmic fit of the velocity profile and the *Shao and Yang* [2008] method yield a ratio which is too low ($\alpha_D/\alpha_S$ is, respectively, 18, 6, and 18%), which means that these methods predict too high an effect of the vegetation density on $\alpha$. Finally, the Reynolds stress method predicts a ratio which is too high (87%) which means that it does not account enough for the influence of the vegetation density on $\alpha$. The methods based on velocity and Reynolds stress profiles do no perform well according to the selection criteria. Using more than one profile could help constrain the shear stress in the heterogeneous flow field explored here and possibly improve their performance.

Only two methods meet all the three proposed criteria: the *Einstein and Banks* [1950] method and the bed load formula inversion. The average value for the $\alpha$ ratio obtained with these methods is 14.3% for the sparse vegetation, and 11.1% for the dense vegetation. Inverting bed load formulas requires that bed load transport measurements be available. This could be specifically useful for a calibration/prediction procedure: available bed load measurements, which are generally limited in space and time, can be used to estimate a value for $\alpha$ (using the bed load transport equation method for instance), which can then be inserted

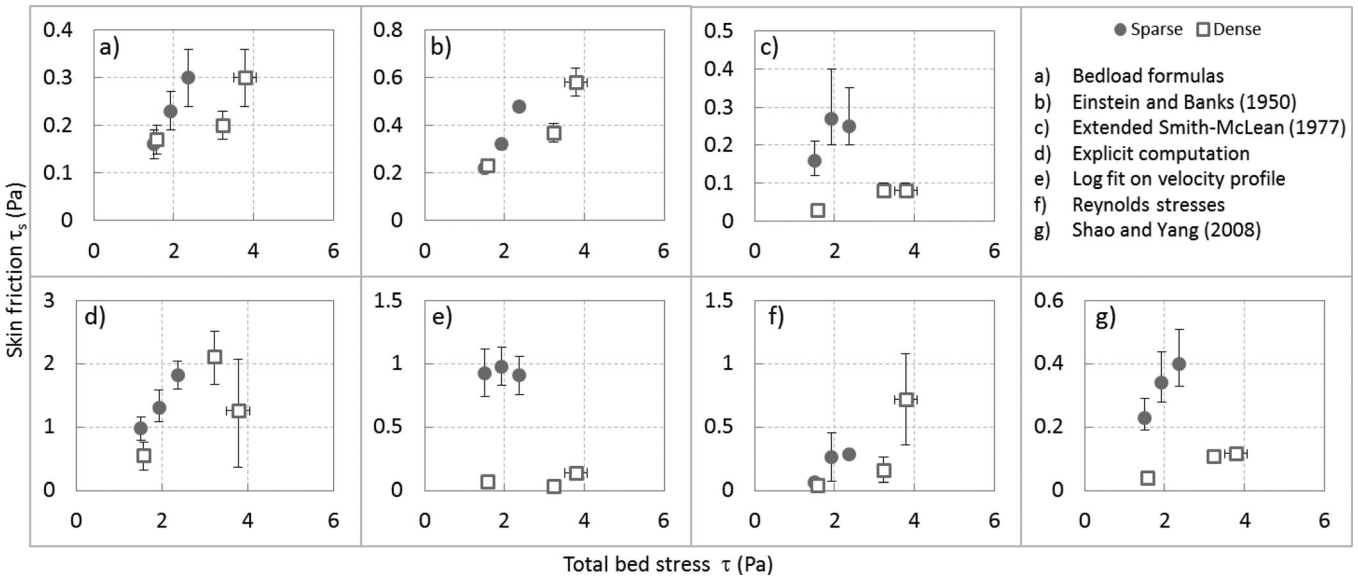


**Figure 8.** Skin stress $\tau_s$ as a function of total bed stress $\tau$ for all the partitioning methods that were tested.

in a model for predicting skin friction and bed load transport on larger space and time scales with changing hydrodynamic conditions (such as a tide cycle and a flood). This procedure is expected to work as long as $\alpha$ depends only on vegetation characteristics (density and shape) and not on the hydrodynamic conditions, as shown above. On the other hand, the *Einstein and Banks* [1950] method does not require many assumptions about the flow. We therefore conclude that inverting bed load formulas to get the skin friction is a reasonable method when bed load transport rates are well constrained and that *Einstein and Banks* [1950] method should be used otherwise.

### 6.3. Implications for Morphodynamic Modeling

Our results could help improve the representation of vegetation in large-scale morphodynamic models. Such models often rely on a 2-D depth-averaged description of the flow where bottom friction is parameterized through a unique coefficient (e.g., Mannings n, the Chezy coefficient, and Darcy Weisbach friction factor). Previous approaches to model flow through vegetation were mostly focused on quantifying the appropriate friction coefficient to account for the effect of the increased resistance to the flow due to the plants. Such correction is appropriate to model the flow but not the sediment transport, because the equations for the flow are based on a total bed stress while the equations for bed load transport are based on the skin stress, which differs from the total bed stress when vegetation is present. With an increased friction coefficient, the hydrodynamic computation predicts correctly a lower flow velocity. However, for an imposed discharge (tidal flow or flood simulation), it also predicts a higher flow depth, hence a higher total bed stress, leading to an overprediction of the sediment transport if no partitioning is performed. It is then necessary to decouple the effects of vegetation: (1) an increase of the total bed stress (related to the increase in the total resistance opposed to the water flow) and (2) a decrease in the skin friction, hence of the bed load transport. Two corrections are therefore needed: (1) an increase of the roughness coefficient (hence of the total bed stress) to account for the effect of the vegetation on the flow, and (2) a correction to extract the skin stress, which is smaller when vegetation is present, to account for the effect of the vegetation on the sediment transport. Most previously published work (starting with *Ree* [1949]) focused on the first type of correction. The second type of correction was introduced for sediment transport with bed forms [*Einstein and Banks*, 1950; *Smith and McLean*, 1977] and for aerial vegetation [*Raupach*, 1992] but has not been commonly used for submerged vegetation [*Jordanova and James*, 2003; *Li and Xie*, 2011].

The parameter $\alpha$ that we propose to use allows coupling the skin friction value (needed for the morphodynamic computation) and the total bed stress (provided by the hydrodynamic computation), hence better representing the effects of vegetation on morphodynamics. This could be implemented simply as follows: first, the total bed stress can be calculated based on a friction law. This total bed stress is used for hydraulic computation. Then, this total bed stress value can be multiplied by the $\alpha$ parameter to obtain the skin friction, i.e., the portion of the total bed stress that is available for sediment transport. This last value can be used for the morphodynamic computations. While our experiments can help choosing a value of the parameter $\alpha$, testing a larger range of plant densities is required to better constrain the relation between $\alpha$ and the plant density.

## 7. Conclusions

We performed a set of experiments to investigate the effect of a plant patch on sediment transport and morphodynamics. Sediment transport appears to be reduced in the plant patch, which triggers a morphodynamic response of the sand bed. The morphodynamic response is characterized by an increase of the bed slope in the plant patch. We suggest that this increase of the bed slope is a response of the bed to compensate for the reduced skin friction and to accommodate the uniform sediment flux expected in a recirculating system. Both the hydrodynamic and morphodynamic effects are larger for the dense patch than for the sparse one. While equilibrium sediment fluxes are similar in both cases, equilibrium slopes and total bed stresses are much higher in the dense patch.

We investigated various shear stress partitioning methods to extract the skin friction component. All methods show that the skin friction is reduced in the plant patch, reducing the sediment transport capacity of the vegetated flow. This effect is stronger for dense vegetation than for sparse. Among all the methods, the inversion of bed load transport formulas and the *Einstein and Banks* [1950] method appeared to produce

the most reasonable values of the skin friction. It appears that the parameter that governs the morphodynamic response of the bed is the ratio of the skin friction to the total bed stress ($\alpha$). This parameter depends on the plant density and is independent of the flow velocity, at least in the range of values tested.

Future work requires testing these predictions at the field scale, investigating a larger range of plant densities, shapes, and mechanical properties to better constrain the relation between $\alpha$ and the plant characteristics, and incorporating this relation into large-scale morphodynamic models to improve the representation of the vegetation.

## Appendix A: Tables of Results From All the Partitioning Methods

This appendix includes one table for each partitioning method that was tested with all the values of $\tau_s$ and $\alpha$ calculated according to this method (Tables A1 and A2).

## Notation

| | |
|---|---|
| $a$ | plant frontal density. |
| $C_{bf}$ | drag coefficient for the bed forms. |
| $C_f$ | total resistance coefficient. |
| $C_{fs}$ | resistance coefficient due to the skin friction only. |
| $C_p$ | drag coefficient for the plants. |
| $C_r$ | drag coefficient associated with the roughness elements (plants and bed forms). |
| $D_{50}$ | median grain size for the sand. |
| $Fr$ | Froude number. |
| $g$ | gravitational acceleration. |
| $h$ | water depth. |
| $H_s$ | equilibrium water depth for the same U but without plants. |
| $h_{max}$ | maximum height above the bed used for fitting a logarithmic law to the velocity profiles. |
| $h_p$ | plant deflected height. |
| $k_s$ | sandbed roughness. |
| $Q$ | flume water discharge. |
| $Q_s$ | total sediment discharge. |
| $Q_{sb}$ | bed load discharge. |
| $Q_{ss}$ | suspended load discharge. |
| $R$ | hydraulic radius. |
| $R_s$ | hydraulic radius associated with water depth $H_s$. |
| $Re$ | Reynolds number. |
| $Re_g$ | grain-related Reynolds number. |
| $S_b$ | bed slope. |
| $S_w$ | water surface slope. |
| $U$ | mean flow velocity. |
| $u'$ and $w'$ | streamwise and vertical components of the fluctuating velocity. |
| $u*$ | shear velocity. |
| $U_p$ | mean velocity in $k_s < z < h_p$. |
| $U_{bf}$ | mean velocity in $k_s < z < \Delta$. |
| $W$ | flume width. |
| $x$ | distance along the streamwise direction. |
| $\alpha$ | ratio of the skin friction and total bed stress. |
| $\alpha_D$ | value of $\alpha$ in the dense vegetation. |
| $\alpha_S$ | value of $\alpha$ in the sparse vegetation. |
| $\Delta$ | ripple height. |
| $\kappa$ | Von Karman constant. |
| $\lambda$ | ripple length. |
| $\nu$ | water kinematic viscosity. |

| | |
|---|---|
| $\rho$ | water density. |
| $\tau$ | total bed stress. |
| $\tau*$ | Shields number (dimensionless shear stress). |
| $\tau_{bf}$ | form drag generated by the bed forms. |
| $\tau_p$ | form drag generated by the plants. |
| $\tau_s$ | skin friction. |
| $\tau(z)$ | shear stress field in the flow. |

**Acknowledgments**
The data that were used for this paper can be made available upon request from the corresponding author. This project was funded by a fellowship from MITACS Canada and Northwest Hydraulic Consultants Ltd. We thank Dave McLean and Derek Ray for their encouragement to work on the problem. We also thank Jacqui Brown and Malcolm Little for their help in the laboratory and Mike Church for critical reviews of the manuscript.

## References

Abdelrhman, M. (2003), Effect of eelgrass *Zostera marina* canopies on flow and transport, *Mar. Ecol. Prog. Ser.*, *248*, 67–83, doi:10.3354/meps248067.
Ackers, P., and W. White (1973), Sediment transport: New approach and analysis, *J. Hydraul. Div. Am. Soc. Civ. Eng.*, *99*, 2041–2060.
Ashida, K., and M. Michiue (1972), Study on hydraulic resistance and bedload transport rate in alluvial streams, *Trans. Jpn. Soc. Civ. Eng.*, *206*, 59–69.
Bos, A., T. Bouma, G. de Kort, and M. van Katwijk (2007), Ecosystem engineering by annual intertidal seagrass beds: Sediment accretion and modification, *Estuarine Coastal Shelf Sci.*, *74*(1–2), 344–348.
Bouma, T., L. van Duren, S. Temmerman, T. Claverie, A. Blanco-Garcia, T. Ysebaert, and P. Herman (2007), Spatial flow and sedimentation patterns within patches of epibenthic structures: Combining field, flume and modelling experiments, *Cont. Shelf Res.*, *27*(8), 1020–1045, doi:10.1016/j.csr.2005.12.019.
Brookshire, E., and K. Dwire (2003), Controls on patterns of coarse organic particle retention in headwater streams, *J. North Am. Benthol. Soc.*, *22*(1), 17–34.
Brownlie, W. R. (1981), Prediction of flow depth and sediment discharge in open channels, technical report KH-R-43A, Keck Lab. of Hydraul. and Water Resour., Calif. Inst. of Technol., Pasadena, Calif.
Brunet, Y., J. Finnigan, and M. Raupach (1994), A wind-tunnel study of air-flow in waving wheat—Single point velocity statistics, *Boundary Layer Meteorol.*, *70*(1–2), 95–132, doi:10.1007/BF00712525.
Carollo, F., V. Ferro, and D. Termini (2002), Flow velocity measurements in vegetated channels, *J. Hydraul. Eng.*, *128*(7), 664–673, doi:10.1061/(ASCE)0733–9429(2002)128:7(664).
Chambers, P., and E. Prepas (1994), Nutrient dynamics in riverbeds: The impact of sewage effluent and aquatic macrophytes, *Water Res.*, *28*(2), 453–464.
Chen, S., H. Chan, and Y. Li (2012), Observations on flow and local scour around submerged flexible vegetation, *Adv. Water Resour.*, *43*, 28–37.
Chen, S.-C., Y.-M. Kuo, and Y.-H. Li (2011), Flow characteristics within different configurations of submerged flexible vegetation, *J. Hydrol.*, *398*(1–2), 124–134, doi:10.1016/j.jhydrol.2010.12.018.
Chen, Z., C. Jiang, and H. Nepf (2013), Flow adjustment at the leading edge of a submerged aquatic canopy, *Water Resour. Res.*, *49*, 5537–5551, doi:10.1002/wrcr.20403.
Church, M. (2006), Bed material transport and the morphology of alluvial river channels, *Annu. Rev. Earth Planet. Sci.*, *34*, 325–354.
Colombini, M., G. Seminara, and M. Tubino (1987), Finite amplitude alternate bars, *J. Fluid Mech.*, *181*, 213–232.
D'Alpaos, A., S. Lanzoni, M. Marani, and A. Rinaldo (2007), Landscape evolution in tidal embayments: Modeling the interplay of erosion, sedimentation, and vegetation dynamics, *J. Geophys. Res.*, *112*, F01008, doi:10.1029/2006JF000537.
Dunn, C., F. Lopez, and M. H. Garcia (1996), Mean flow and turbulence in a laboratory channel with simulated vegetation, technical report, U.S. Army Corps of Eng. Hydraulic Engineering Studies no 51.
Einstein, H. A., and R. B. Banks (1950), Fluid resistance of composite roughness, *Trans. AGU*, *31*(4), 603–610.
Engelund, F., and J. Fredsoe (1976), A sediment transport model for straight alluvial channels, *Nord. Hydrol.*, *7*, 293–306.
Engelund, F., and E. Hansen (1967), *A Monograph on Sediment Transport in Alluvial Streams*, Tech. Vorlag, Copenhagen.
Fernandez-Luque, R., and R. Van Beek (1976), Erosion and transport of bedload sediment, *J. Hydraul. Res.*, *14*(2), 127–144.
Fischenich, J. (1997), Hydraulic impacts of riparian vegetation: Summary of the literature, *Tech. Rep. EL-97-9*, U.S. Army Corps of Eng. Vicksburg, Miss.
Folkard, A. M. (2011), Flow regimes in gaps within stands of flexible vegetation: Laboratory flume simulations, *Environ. Fluid Mech.*, *11*(3), 289–306, doi:10.1007/s10652-010-9197-5.
Follett, E., and H. Nepf (2012), Sediment patterns near a model patch of reedy emergent vegetation, *Geomorphology*, *179*, 141–151.
Fonseca, M., J. Fisher, J. Zieman, and G. Thayer (1982), Influence of the seagrass, *Zostera marina* L., on current flow, *Estuarine Coastal Shelf Sci.*, *15*(4), 351–364, doi:10.1016/0272-7714(82)90046-4.
Fonseca, M., J. Zieman, G. Thayer, and J. Fisher (1983), The role of current velocity in structuring seagrass meadows, *Estuarine Coastal Shelf Sci.*, *17*, 367–380.
Friedrichs, C. T., and J. E. Perry (2001), Tidal salt marsh morphodynamics: A synthesis, *J. Coastal Res.*, *27*, 7–37.
Ghisalberti, M., and H. Nepf (2002), Mixing layers and coherent structures in vegetated aquatic flows, *J. Geophys. Res.*, *107*(C2), doi:10.1029/2001JC000871.
Ghisalberti, M., and H. Nepf (2006), The structure of the shear layer in flows over rigid and flexible canopies, *Environ. Fluid Mech.*, *6*(3), 277–301, doi:10.1007/s10652-006-0002–4.
Gran, K., and C. Paola (2001), Riparian vegetation controls on braided stream dynamics, *Water Resour. Res.*, *37*(12), 3275–3283.
Jarvela, J. (2002), Flow resistance of flexible and stiff vegetation: A flume study with natural plants, *J. Hydrol.*, *269*(1–2), 44–54, doi:10.1016/S0022-1694(02)00193-2.
Jarvela, J. (2005), Effect of submerged flexible vegetation on flow structure and resistance, *J. Hydrol.*, *307*(1–4), 233–241, doi:10.1016/j.jhydrol.2004.10.013.
Jordanova, A. A., and C. S. James (2003), Experimental study of bedload transport through emergent vegetation, *J. Hydraul. Eng.*, *129*, 474–478.
Kirwan, M. L., and A. B. Murray (2007), A coupled geomorphic and ecological model of tidal marsh evolution, *Proc. Natl. Acad. Sci. U. S. A.*, *104*, 6118–6122, doi:10.1073/pnas.0700958104.

Koch, E. (2001), Beyond light: Physical, geological, and geochemical parameters as possible submersed aquatic vegetation habitat requirements, *Estuaries*, *24*(1), 1–17, doi:10.2307/1352808.
Lacy, J. R., and S. Wyllie-Echeverria (2011), The influence of current speed and vegetation density on flow structure in two macrotidal eelgrass canopies, *Limnol. Oceanogr. Fluids Environ.*, *1*, 38–55, doi:10.1215/21573698-1152489.
Larsen, L., J. Harvey, and J. Crimaldi (2009), Predicting bed shear stress and its role in sediment dynamics and restoration potential of the everglades and other vegetated flow systems, *Ecol. Eng.*, *35*(12), 1773–1785.
Le Bouteiller, C., and J. G. Venditti (2014), Vegetation-driven morphodynamic adjustments of a sand bed, *Geophys. Res. Lett.*, *41*, 3876–3883, doi:10.1002/2014GL060155.
Lefebvre, A., C. Thompson, and C. Amos (2010), Influence of *Zostera marina* canopies on unidirectional flow, hydraulic roughness and sediment movement, *Cont. Shelf Res.*, *30*(16), 1783–1794, doi:10.1016/j.csr.2010.08.006.
Li, C. W., and J. F. Xie (2011), Numerical modeling of free surface flow over submerged and highly flexible vegetation, *Adv. Water Resour.*, *34*(4), 468–477, doi:10.1016/j.advwatres.2011.01.002.
Madsen, J. B., P. Chambers, W. James, E. Koch, and D. Westlake (2001), The interaction between water movement, sediment dynamics and submersed macrophytes, *Hydrobiologia*, *444*, 71–84.
Marani, M. B., A. D'Alpaos, S. Lanzoni, L. Carniello, and A. D. Rinaldo (2010), The importance of being coupled: Stable states and catastrophic shifts in tidal biomorphodynamics, *J. Geophys. Res.*, *115*, F04004, doi:10.1029/2009JF001600.
Moore, K. (2004), Influence of seagrasses on water quality in shallow regions of the lower chesapeake bay, *J. Coastal Res.*, *20*(45), 162–178.
Nelson, J., S. McLean, and S. Wolfe (1993), Mean flow and turbulence fields over two-dimensional bed forms, *Water Resour. Res.*, *29*(12), 3935–3953.
Nepf, H., and M. Ghisalberti (2008), Flow and transport in channels with submerged vegetation, *Acta Geophys.*, *56*(3), 753–777, doi:10.2478/s11600-008-0017-y.
Nepf, H. M. (2012), Flow and transport in regions with aquatic vegetation, *Annu. Rev.*, *44*, 123–142.
Nepf, H. M., and E. R. Vivoni (2000), Flow structure in depth-limited, vegetated flow, *J. Geophys. Res.*, *105*(C12), 28,547–28,558, doi:10.1029/2000JC900145.
Nezu, I., and K. Onitsuka (2001), Turbulent structures in partly vegetated open-channel flows with LDA and PIV measurements, *J. Hydraul. Res.*, *39*(6), 629–642.
Nino, Y., and M. Garcia (1998), Using Lagrangian particle saltation observations for bedload sediment transport modelling, *Hydrol. Processes*, *12*(8), 1197–1118.
Okamoto, T.-A., I. Nezu, and H. Ikeda (2012), Vertical mass and momentum transport in open-channel flows with submerged vegetations, *J. Hydro-environ. Res.*, *6*(4), 287–297.
Perignon, M. C., G. E. Tucker, E. R. Griffin, and J. M. Friedman (2013), Effects of riparian vegetation on topographic change during a large flood event, Rio Puerco, New Mexico, USA, *J. Geophys. Res.*, *118*, 1193–1209, doi:10.1002/jgrf.20073.
Poggi, D., A. Porporato, L. Ridolfi, J. Albertson, and G. Katul (2004), The effect of vegetation density on canopy sub-layer turbulence, *Boundary Layer Meteorol.*, *111*(3), 565–587, doi:10.1023/B:BOUN.0000016576.05621.73.
Raupach, M. (1992), Drag and drag partition on rough surfaces, *Boundary Layer Meteorol.*, *60*(4), 375–395, doi:10.1007/BF00155203.
Raupach, M., and A. Thom (1981), Turbulence in and above plant canopies, *Annu. Rev. Fluid Mech.*, *13*, 97–129, doi:10.1146/annurev.fl.13.010181.000525.
Raupach, M., J. Finnigan, and Y. Brunet (1996), Coherent eddies and turbulence in vegetation canopies: The mixing-layer analogy, *Boundary Layer Meteorol.*, *78*(3–4), 351–382, doi:10.1007/BF00120941.
Ree, W. (1949), Hydraulic characteristics of vegetation for vegetated waterways, *Agric. Eng.*, *30*, pp. 184–189, Stillwater, Okla.
Ree, W. (1954), Handbook of channel design for soil and water conservation, *Tech. Rep. SCS-TP-61*, Soil Conserv. Serv.—USDA.
Sand-Jensen, K. (1998), Influence of submerged macrophytes on sediment composition and near-bed flow in lowland streams, *Freshwater Biol.*, *39*(4), 663–679.
Shao, Y., and Y. Yang (2008), A theory for drag partition over rough surfaces, *J. Geophys. Res.*, *113*, F02S05, doi:10.1029/2007JF000791.
Smith, J. D., and S. R. McLean (1977), Spatially averaged flow over a wavy surface, *J. Geophys. Res.*, *82*(12), 1735–1746.
Souliotis, D., and P. Prinos (2011), Effect of a vegetation patch on turbulent channel flow, *J. Hydraul. Res.*, *49*(2), 157–167, doi:10.1080/00221686.2011.557258.
Stephan, U., and D. Gutknecht (2002), Hydraulic resistance of submerged flexible vegetation, *J. Hydrol.*, *269*(1–2), 27–43, doi:10.1016/S0022-1694(02)00192-0.
Tal, M., and C. Paola (2007), Dynamic single-thread channels maintained by the interaction of flow and vegetation, *Geology*, *35*(4), 347–350.
Temmerman, S., T. J. Bouma, J. Van de Koppel, D. Van der Wal, M. B. De Vries, and P. M. J. Herman (2007), Vegetation causes channel erosion in a tidal landscape, *Geology*, *35*(7), 631–634, doi:10.1130/G23502A.1.
Van Rijn, L. (1984), Sediment transport, Part I: Bed load transport, *J. Hydraul. Eng.*, *110*(10), 1431–1456.
Vanoni, V. A., and N. H. Brooks (1957), Laboratory studies of the roughness and suspended load of alluvial streams, technical report E-68, U.S. Army Corps of Eng, Calif. Inst. of Technol., Pasadena, Calif.
Wiberg, P., and J. Nelson (1992), Unidirectional flow over asymmetric and symmetric ripples, *J. Geophys. Res.*, *97*(C8), 12,745–12,761.
Wilson, K. (1966), Bed load transport at high shear stresses, *J. Hydraul. Div. Am. Soc. Civ. Eng.*, *92*(6), 49–59.
Wu, F., H. Shen, and Y. Chou (1999), Variation of roughness coefficient for unsubmerged and submerged vegetation, *J. Hydraul. Eng.*, *125*(9), 934–941.
Wu, W., and Z. He (2009), Effects of vegetation on flow conveyance and sediment transport capacity, *Int. J. Sediment Res.*, *24*(3), 247–259.
Yager, E. M., and M. W. Schmeeckle (2013), The influence of vegetation on turbulence and bed load transport, *J. Geophys. Res. Earth Surf.*, *118*, 1585–1601, doi:10.1002/jgrf.20085.
Zong, L., and H. Nepf (2011), Spatial distribution of deposition within a patch of vegetation, *Water Resour. Res.*, *470*, W03516, doi:10.1029/2010WR009516.